Electronic Supplementary Information

Unprecedented Energy Storage in Metal-Organic Complexes via Constitutional Isomerism

Alagar Raja Kottaichamy,[a] Siraprapha Deebansok,[b] Jie Deng,[c] Mohammed Azeezulla Nazrulla,[d] Yachao Zhu,[e] Zahid Manzoor Bhat,[a] Mruthyunjayachari Chattanahalli Devendrachari,[a] Chathakudath Prabhakaran Vinod,[f] Harish Makri Nimbegondi Kotresh,*[g] Olivier Fontaine*[b, h] and Musthafa Ottakam Thotiyl*[a]

[a] Indian Institute of Science Education and Research (IISER) Pune, Dr. Homi Bhabha Road, Pashan, Pune, 411008, India.

[b] Molecular Electrochemistry for Energy Laboratory, VISTEC, Rayong, 21210, Thailand.

[c] Institute for Advanced Study & College of Food and Biological Engineering, Chengdu University, Chengdu 610106, China.

[d] Department of Materials Chemistry, National Institute of Chemistry, 1000 Ljubljana, Slovenia.

[e] ICGM, Univ. Montpellier, CNRS, ENSCM, 34293 Montpellier, France.

[f] Catalysis and Inorganic Chemistry Division, CSIR-NCL, Pune 411008, India.

[g] Department of Chemistry, Acharya Institute of Technology, Soldevanahalli, Bangalore-560107, India.

[h] Institut Universitaire de France, 75005 Paris, France.

Contents

1. Materials and Methods

a. Chemicals

The chemicals such as N,N dimethylformamide (DMF) (99%), hexane (95%), isopropyl alcohol (99%), isopropyl alcohol (99%), cobalt (II) chloride hexahydrate (≥98%), nickel (II) chloride hexahydrate (≥98%), copper (II) chloride dehydrate (≥98%), zinc (II) chloride hydrate (99.99%) ($ZnCl_2$), ammonium molybdate (99.99%), 4-nitrophthalimide (98%), 3-nitrophthalimide (98%), sodium sulfide nonahydrate (≥98%), ammonium chloride (≥98%), toluene (99.5%), methanol (99%), ethanol (95%), sulfuric acid (96%), potassium phosphate dibasic (K_2HPO_4) (98%), potassium phosphate monobasic (KH_2PO_4) (99%), and nitrobenzene (99%) were procured from Alfa Aesar, India. Dimethyl sulfoxide-d_6 (DMSO-d_6) (99.9 atom % D), sodium acetate (≥99%), sodium hydroxide (≥99%), hydrogen peroxide (30 %), hydrochloric acid (37.0%) and Nafion solutions (5 wt %) were procured from Sigma-Aldrich, India. The YP-50F carbon was purchased from Kuraray chemicals, India.

b. Characterization techniques

UV-Visible measurements of alpha and beta Tetraaminophthalocyanatometal (II) (TAMPc) (Metal (M) - Co, Ni, Cu, Zn) were carried out in a quartz cuvette using a Perkin Elmer Lambda 950 instrument. FTIR spectra of alpha and beta TAMPc (M- Co, Ni, Cu, Zn), TACoPc anchored on YP-50F was collected using a Bruker Alpha ATR-FTIR. Scanning electron microscopy with an energy dispersive X-ray spectrum (Zeiss Ultraplus-4095). Raman spectra of alpha and beta TAMPc (M- Co, Ni, Cu, Zn) were recorded using a Raman microscope (LabRAM HR, Horbia Jobin Yvon). Nuclear magnetic resonance (NMR) spectra of alpha and beta TAZnPc were recorded with Bruker 400 MHz spectrometer. Transmission electron microscopy (TEM) was carried out in a Tecnai T12 G2 TWIN operated at $U_0 = 120$ kV. X-ray photo electron spectroscopy (XPS) was carried out using Thermo Scientific Kalpha+ spectrometer. The measurements were carried out using a monochromated Al Kα (1486.6 eV) X-ray source with 72 W power. The spot size of the X-rays were 400 µm. For electron energy analysis a 180^0 double focusing hemispherical analyzer with 128 channel detector was used. An ultra-low energy co-axial electron beam and Ar^+ ion beam was used for charge compensation and the charge compensation gun was switched on during the spectral acquisition. The final spectra were cross verified for charge accumulation with C1s standard value at 284.6 eV. The base pressure of the spectrometer was always better than ~$5x10^{-9}$ mbar

(gun vacuum) and ~$1x10^{-7}$ mbar (system vacuum) during data acquisition with flood gun on. The survey scan was collected at 200 eV pass energy and individual core-levels at 50 eV. Peak fitting of N1s spectra was carried out using Avantage software with a smart background.

c. Electrochemical techniques

The electrochemical experiments were carried out using Biologic VMP 300 potentiostat. A double jacketed three-electrode cell (10 ml volume) configuration with a 3 mm diameter glassy carbon disk as the working electrode and a platinum wire as the counter electrode was employed for electrochemical measurements. $Hg/Hg_2SO_4/SO_4^{2-}$ electrode was used for acidic pH and $Hg/HgO/OH^-$ electrode was used for alkaline pH as the reference electrodes. All the potentials were finally converted to reversible hydrogen scale (RHE scale) based on the redox potentials for hydrogen redox reactions in respective electrolytes obtained on a Pt disc working electrode. All solutions were prepared using Millipore water (18.2 MΩ.cm) and the cell temperature was maintained at 25˚C using a water bath fitted with a temperature controller**.**

The electrode surface was cleaned by 0.05 μM of alumina powder by polishing. Each time before the measurement, electrochemical cycling was carried out in the respective electrolytes for electrochemically cleaning the surface. Impedance was acquired in the frequency range of 100 kHz to 5 mHz with an AC amplitude of 10 mV (peak to peak) at a bias voltage of 0 V vs. OCV in N_2 saturated solutions. The TACoPc@YP-50F (composite with activated carbon YP-50F) modified glassy carbon electrodes were prepared by the drop-casting method. A homogeneous dispersion was prepared by sonicating a known amount of catalysts (α-TACoPc isomer, and β-TACoPc isomer composite with activated carbon YP-50F) in isopropyl alcohol (IPA) with 5 wt% Nafion as the binder to prepare the composite ink.

2. Synthesis of TNMPc/TAMPc

a. Synthesis of 1,8,15,22 Tetranitrophthalocyanatocobalt (II) (*α*-TNCoPc) / 2,9,16,23-Tetraanitrophthalocyanatocobalt (II) (*β*-TNCoPc)

Synthesis of 2,9,16,23-Tetranitro cobalt phthalocyanine / 1,8,15,22- Tetranitro cobalt phthalocyanine was done according to the literature.[1,2] A 250 ml round-bottomed flask was charged with a finely grounded mixture of 4-nitro phthalimide / 3-nitro phthalimide (3.86 g),

Urea (6.0 g), ammonium molybdate (0.05 g) as a catalyst, ammonium chloride (0.5 g) and 30 ml of nitrobenzene. The reaction mixture was stirred for 10 minutes to get a homogeneous mixture and then added cobalt (II) chloride as the metal salt (1.2 g) followed by subsequent vigorous stirring at 100^{o}C for about 30 minutes. Then the temperature was increased to 180^{o}C at the rate of 10^{o}C/30 minutes and refluxed the reaction mixture at 180^{o}C for about 4 hours. The mixture was diluted with toluene (50 ml) and the resulting precipitate was filtered, washed thoroughly with hot water and methanol and finally washed with hexane and then dried in an oven at 80^{o}C.

b. Preparation of 1,8,15,22 Tetraaminophthalocyanatocobalt (II) / 2,9,16,23-Tetraaminophthalocyanatocibalt (II) from 1,8,15,22-Tetranitrophthalocyanatocobalt (II) / 2,9,16,23-Tetranitrophthalocyanatocobalt (II)

A 250 ml round-bottomed flask was charged with tetra nitro cobalt phthalocyanine (0.75 g), sodium sulfide nonahydrate (3.0 g) and 30 ml of N, N, dimethylformamide. The reaction mixture was heated to 80^{o}C for about 2 hours. It was then cooled to room temperature and diluted with ice water (200 ml), and the resulting precipitate was filtered off and washed thoroughly with hot water followed by methanol and finally with hexane. The obtained precipitate was dried in an oven to obtain cobalt 1,8,15,22- tetraamino cobalt phthalocyanine (α-TACoPc) or 2,9,16,23-tetraamino cobalt phthalocyanine (β-TACoPc).

c. Synthesis of α-TANiPc / β-TANiPc, α-TACuPc / β-TACuPc, and α-TAZnPc / β-TAZnPc

The above same synthetic protocol was followed for the synthesis of α-TANiPc/ β-TANiPc, α-TACuPc/ β-TACuPc and α-TAZnPc/ β-TAZnPc with nickel (II) chloride, copper (II) chloride and zinc chloride ($ZnCl_2$) as the metal salt respectively.

3. Experimental characterization of *α* and *β*-TAMPc isomeric molecules

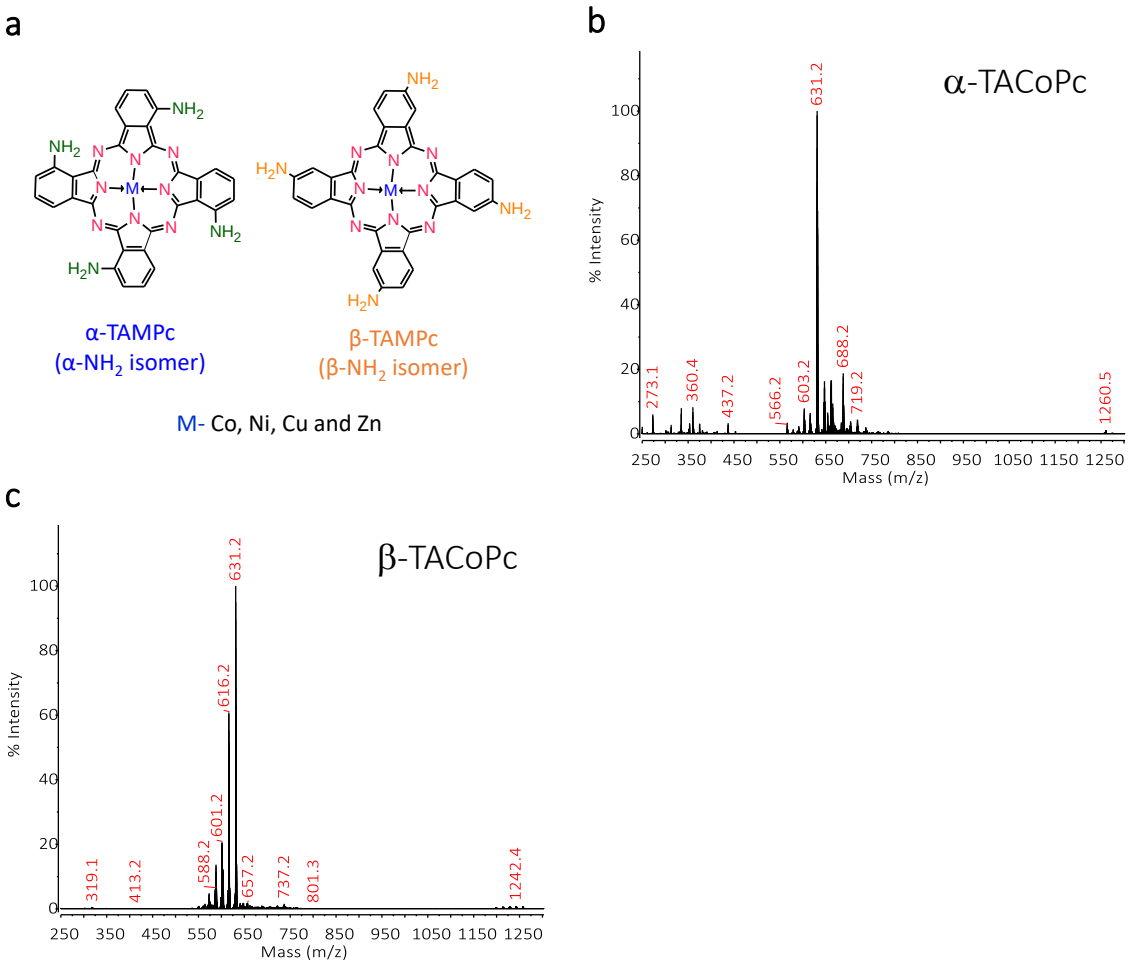

Figure S1 | Molecular structure and TOF mass spectrometry. (a) Molecular structure of *α*-TAMPc and *β*-TAMPc isomeric molecules, where M stands for Co, Ni, Cu, and Zn ions. (b and c) MALDI-TOF of *α*-TACoPc and *β*-TACoPc isomeric molecules.

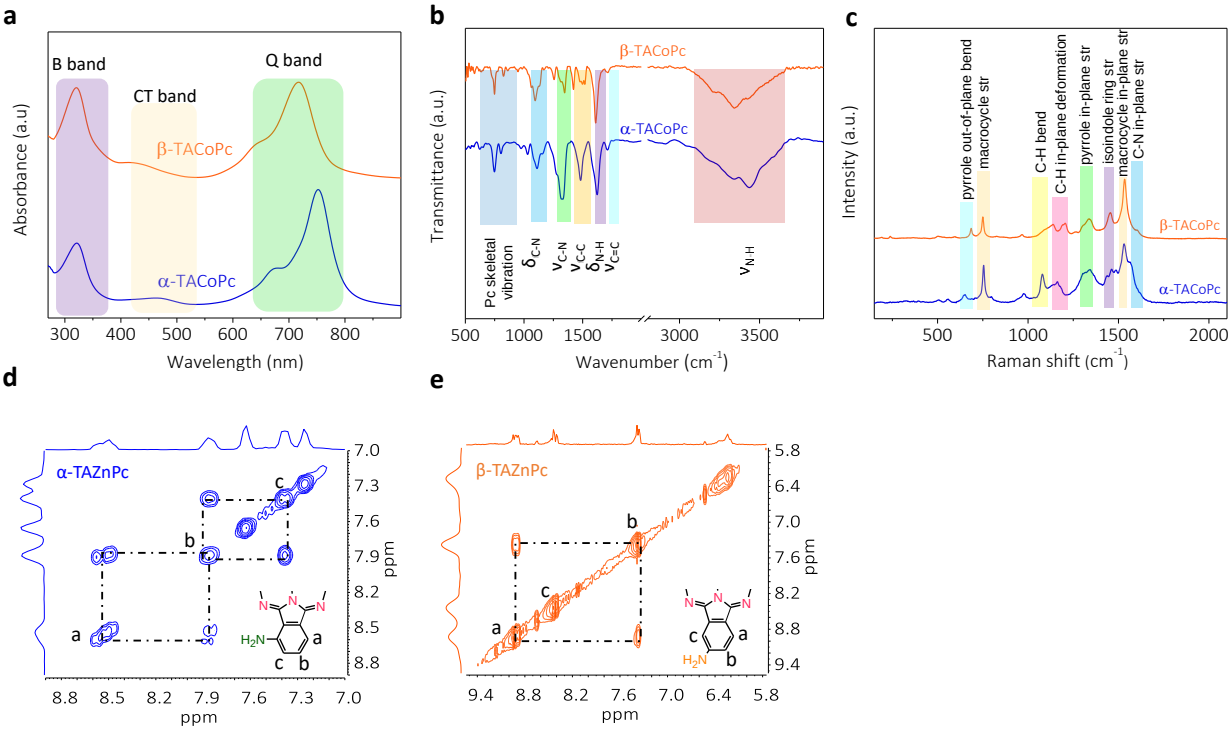

Figure S2 | Spectroscopic Characterization of Ligand Geometry and the associated Charge Delocalization. (a) UV-visible spectroscopy of *α*-TACoPc and *β*-TACoPc isomeric molecules. (b) Fourier transform infra-red (FTIR) spectroscopy and (c) Raman spectroscopy of *α*-TACoPc and *β*-TACoPc isomeric molecules. (d) and (e), 2D Nuclear magnetic resonance (NMR) spectra: ^{1}H-^{1}H Correlation Spectroscopy (COSY) of (c) *α*-TAZnPc and (d) *β*-TAZnPc isomeric molecules.

Taking a cobalt-based system as the model molecule (TACoPc), matrix-assisted laser desorption/ionization time-of-flight mass spectrometry (MALDI-TOF) shows the parent ion peak at an m/z value of ~632 corresponding to the molecular masses of TACoPc, as shown in Figures S1b and S1c. The MALDI-TOF data show the parent ion peak for *α*-TACoPc/*β*-TACoPc at m/z value of ~631 and these correspond to their respective molecular masses. Minor peaks at various m/z values indicate the fragment peaks. UV-Vis spectra of these molecules show the Q- and B-bands to be in the range of 650-800 nm and 200-350 nm (Figure S2a), respectively, which is characteristic of metal phthalocyanines[3,4]A small peak close to 450 nm is attributed to the charge transfer band.[3,4] A comparison between *α*-TACoPc (*α* isomer) and *β*-TACoPc (*β* isomer) isomeric molecules with respect to their UV-Vis spectra suggests a red-shifted Q-band in the former. The Q-band has more ligand-type characteristics[5,6] and this redshift thus indicates comparatively extensive charge delocalization in the *α*-isomer as compared to the *β* isomer.[7,8] FTIR spectra and Raman spectroscopy of the isomeric molecules indicate the successful formation of –NH_2 functionalized phthalocyanine molecules, as shown in Figures S2b and S2c. FTIR spectra of isomeric molecules indicate C-N bond vibration at

~1114 cm^{-1}, aromatic ring vibrations at ~1635 cm^{-1}, phthalocyanine skeletal vibrations in the range 550 cm^{-1} - 930 cm^{-1} and pyrrole ring vibrations at ~1246 cm^{-1}, Figure S1c. The appearance of stretching vibrations in the range 3190 cm^{-1}- 3450 cm^{-1} is indicative of primary amine groups in the isomeric molecules.[9,10] Raman spectra reveal phthalocyanine signature peaks with C-H in plane deformation in the macrocyclic ring at ~1195 cm^{-1} and macrocyclic stretching vibration at ~764 cm^{-1}.[7,11] Stretching vibration of the isoindole ring unit is observed at a Raman shift of ~1456 cm^{-1} and C-N in plane stretching vibrations are observed at ~1404 cm^{-1} and ~1678 cm^{-1},[12,13] Figure S2d.

In order to further verify the formation of amino-based isomeric molecules, Nuclear Magnetic Resonance (NMR) spectroscopy was used. NMR analyses were carried out with the corresponding zinc-based amino phthalocyanines (labelled α-TAZnPc and β-TAZnPc), as cobalt-based amino phthalocyanines are paramagnetic in nature (the synthesis is described in the experimental section, page S5).[14,15] In line with the geometry of the ligands provided in Figure S2d, 2D COSY NMR spectra of the α and β isomers of TAZnPc (Figure S2d and S2e), demonstrate the presence of three different types of aromatic C-H protons, denoted by a, b and c (insets of Figures S2d and S2e). The correlation spectra for α-TAZnPc (Figure S2d) show that the proton corresponding to the chemical shift at 7.86 ppm may couple with the protons at 7.37 ppm and 8.52 ppm. This thus confirms the arrangements of protons in the α molecule, as shown in the inset of Figure S2d. On the other hand, in β-TAZnPc, the chemically shifted protons at 7.38 ppm (labeled as 'b' in the inset of Figure S2e) can only couple with the proton at 8.91 ppm (labeled as 'a' in the inset of Figure S2e) and not with the proton at 8.42 ppm (labeled as 'c' in the inset of Figure S2e). This confirms the arrangement of protons in the β molecule, as shown in inset of Figure S2e. Therefore, the 2D COSY NMR spectra confirm the ligand isomerism in amino-substituted cobalt phthalocyanines, in line with the structures provided in Figure S1a. Similarly, amino-substituted metal phthalocyanines of Ni, Cu and Zn were synthesized and characterized as per the literature[1,2], which are detailed discussed in the following section, Figures S3 and S4.

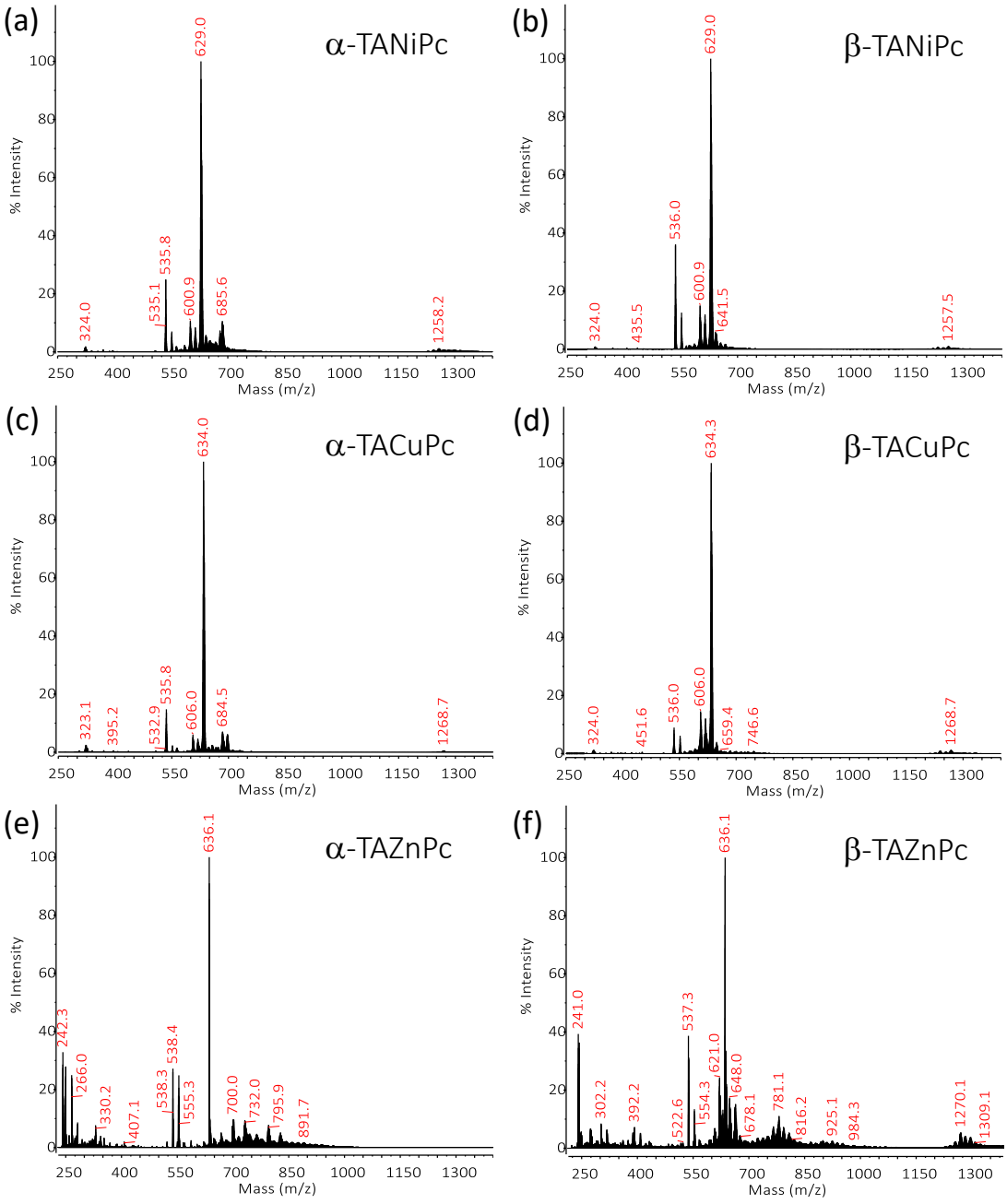

Figure S3 | TOF mass spectrometry analysis. MALDI-TOF of *α* and *β*-TAMPc isomeric molecules (where M = Ni, Cu and Zn). (a, b) *α*-TANiPc and β-TANiPc isomeric molecules, (c, d) *α*-TACuPc and *β*-TACuPc isomeric molecules and (e, f) *α*-TAZnPc and *β*-TAZnPc isomeric molecules.

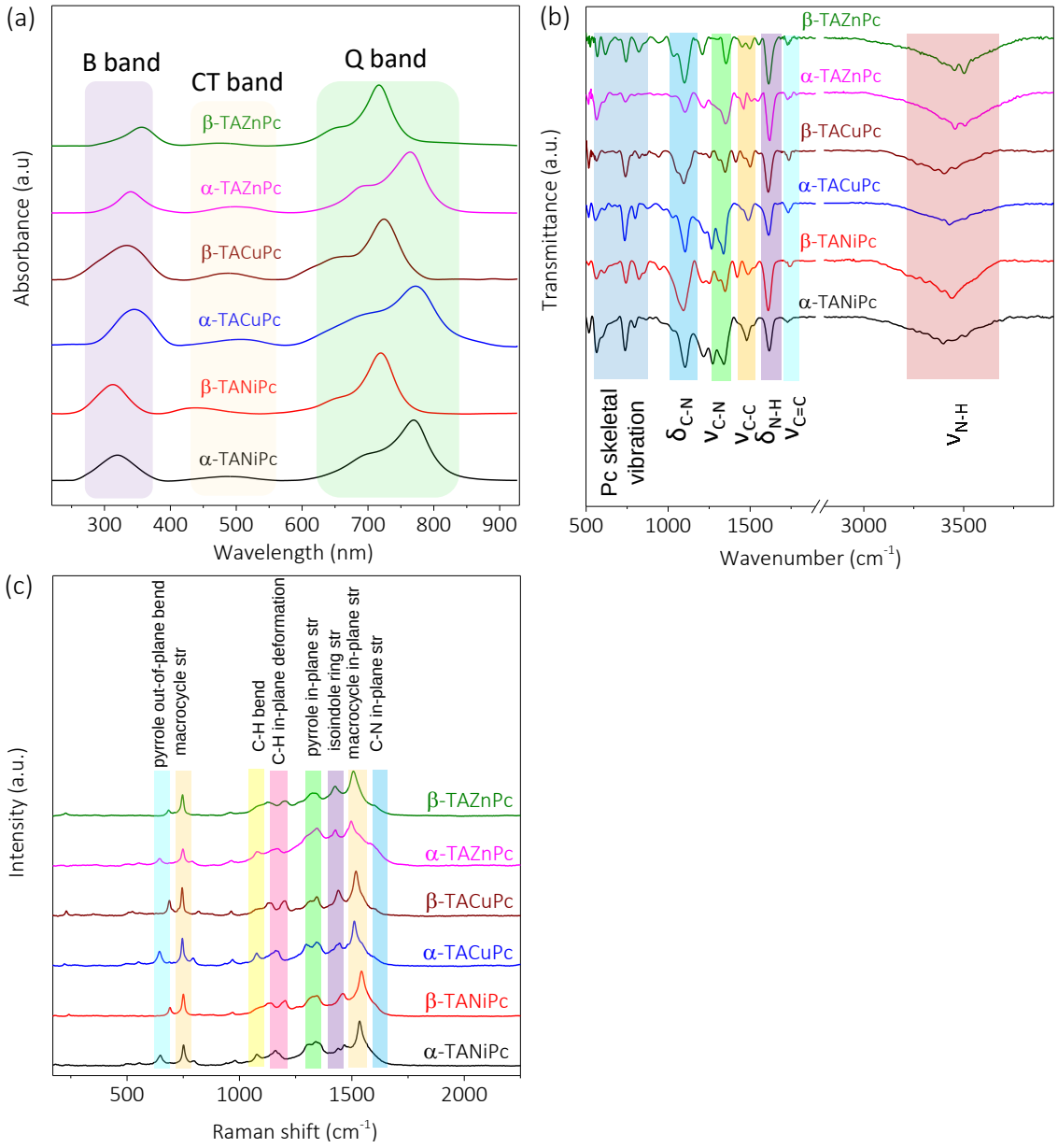

Figure S4 | Spectroscopic analysis. (a) UV-visible spectroscopy, (b) FT-IR spectroscopy and (c) Raman spectroscopy of α-TAMPc and β-TAMPc isomers (where M= Ni, Cu and Zn).

The MALDI-TOF data show the parent ion peak for α-TANiPc/β-TANiPc at m/z value of ~629, the parent ion peak for α-TACuPc/β-TACuPc at m/z value of ~634 and the parent ion peak for α-TAZnPc/β-TAZnPc at m/z value of ~636. These correspond to their respective molecular masses. Minor peaks at various m/z values indicate the fragment peaks. The UV-vis spectra of TAMPc isomers (where M= Ni, Cu and Zn) show Q band, B band and charge transfer bands which are characteristics of phthalocyanines, Figure S4a. It should be noted that in the UV Vis spectral patterns of all the isomeric molecules, the Q band of α isomer demonstrates a red shift with respect to the corresponding β isomer signalling comparatively extensive

electronic delocalization in the former compared to the latter. The appearance of phthalocyanine skeletal vibrations in the range 525-945 cm^{-1}, C-N bond vibration in the range 1000-1165 cm^{-1}, pyrrole ring vibrations in the range 1215-1245 cm^{-1}, aromatic ring vibrations in the range 1620-1640 cm^{-1} and primary amine stretching vibrations in the range 3140-3490 cm^{-1} signal the formation of phthalocyanine molecules, Figure S4b.[9,10] Raman spectra show phthalocyanine signature peaks where the peaks in the 740-765 cm^{-1} range represent the macrocyclic stretching vibration and 1190-1215 cm^{-1} range represent the C-H in plane deformation in the macrocyclic ring.[11,7] The Raman shift in the range 1423-1465 cm^{-1} corresponds to the stretching vibration of the isoindole ring unit, and the Raman shift in the range 1395-1410 cm^{-1} and 1645-1680 cm^{-1} represent the C-N in plane stretching vibrations.[12,13] All these indicate the successful formation of corresponding molecular complexes, Figure S4c. The obvious difference in their spectral behavior with respect different metal centers reflects the influence of the central metal cations (Ni, Cu, Zn).

4. Computational methodology

All the density functional theory (DFT) calculations were performed by employing a hybrid CAM-B3LYP (Coulomb-Attenuating Method, Becke, three-parameter, Lee-Yang-Parr)[16] exchange-correlation functional in Gaussian 09 (Revision C.01) suite of packages.[17] Double zeta valence polarization (dg-DZVP) basis sets have been used for all the atoms, viz., H, C, and N. Unrestricted Kohn-Sham formalism has been utilized for the ground state (GS) optimizations of all the structures under study. Default convergence criterion with Berny algorithm and extra quadratically convergent (XQC) self-consistent field (SCF) method is used for all the GS geometry optimizations (whenever there was a problem with convergence criterion, opt=loose have been employed) and are confirmed as the local minima with all positive vibrational frequencies. The empirical dispersion (iop (3/124=30), Grimme D3, DFT-D3)[18,19] term is included for all the calculations as well for the relative energy. Relative energies ($E_{R.E}$) is calculated using the following equation,

$$E_{R.E} = E_{GS} - E_{HES} \ldots\ldots \text{(S1)}$$

Where, E_{GS} and E_{HES}, respectively are the total corrected energies (free energy) of the ground state (GS) and high energy state (HES). For natural atomic orbital and natural bond orbital analysis (NBO) program of Gaussian NBO Version 3.1[20] have been employed to understand the charge population in all the studies ASMPCs. All images have been plotted from the Gauss View 5.0 and VESTA 3.4.4.[21]

5. Hydrogen bonding and surface charge analysis

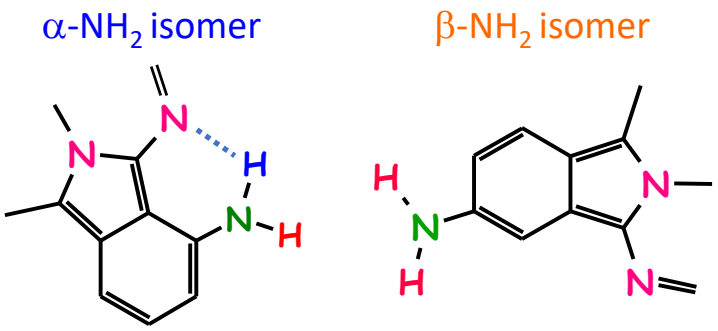

Scheme S1 | H bonding interactions. Scheme showing intramolecular H bonding interactions in α-NH_2 isomer involving imine nitrogen and amine protons. Scheme showing the absence of such hydrogen bonding interactions in β-NH_2 isomer due to the unfavourable positions of H bonding groups.

(a)

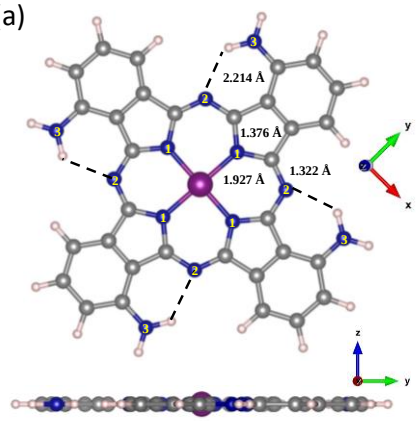

α-TACoPc

(b)

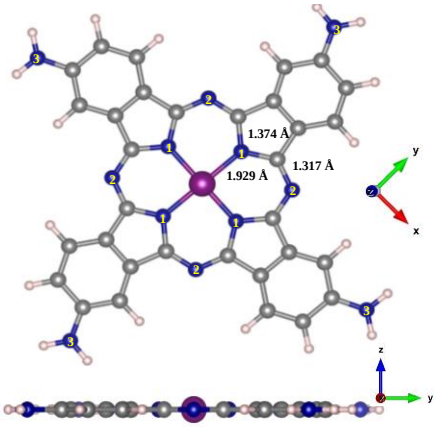

β -TACoPc

4 H⁺ Protonation

(c)

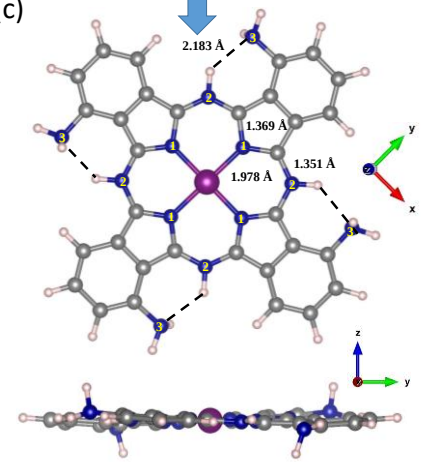

1:4 (molecule to proton)
Protonation of α-TACoPc

4 H⁺ Protonation

(d)

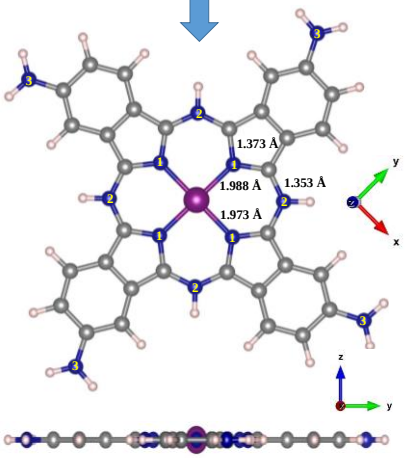

1:4 (molecule to proton)
Protonation of β-TACoPc

4 H⁺ Protonation

(e)

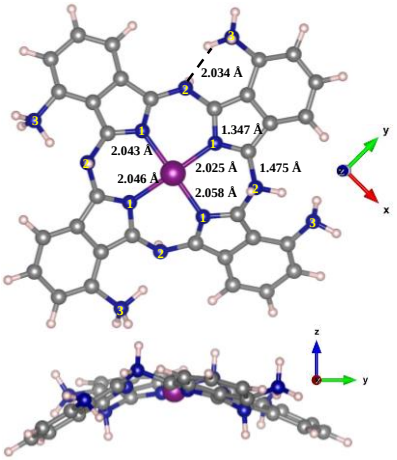

1:8 (molecule to proton)
Protonation of α-TACoPc

4 H⁺ Protonation

(f)

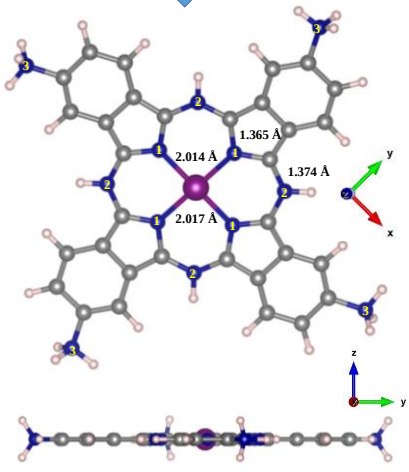

1:8 (molecule to proton)
Protonation of β-TACoPc

Figure S5 | DFT analysis. Stable geometry of pristine (a) *α*-TACoPc and (b) *β*-TACoPc isomers. Stable geometry of protonated (c) *α*-TACoPc and (d) *β*-TACoPc isomers with molecule to proton ratio of 1:4 and stable geometry of protonated (e) *α*-TACoPc and (f) *β*-TACoPc isomers with molecule to proton ratio of 1:8. (Nitrogen atoms are labeled in their stable geometry in Figure S5: N1: pyrrole nitrogen atoms; N2: iminic nitrogen atoms; and N3: nitrogen atom of NH_2 groups)

Table S1 | Comparative parameters from DFT Study (extracted from Figure 1a, 1b and Figure S5).

System		***Parameters***		***Relative energy difference between alpha and beta isomers***
		Hydrogen bond distance (N-H---N)	***Bond angle (N-H---N)***	
Pristine	*α-TACoPc*	*2.225 Å*	*129.75°*	*β-TACoPc* ↕ *0. 87 eV* *α-TACoPc*
	β-TACoPc	-	-	
1:4 (molecule to proton) protonation	*α-TACoPc*	*2.213 Å*	*132.40°*	*β-TACoPc (1:4) protonation* ↕ *2.68 eV* *α-TACoPc (1:4) protonation*
	β-TACoPc	-	-	
1:8 (molecule to proton) protonation	*α-TACoPc*	-	-	*α-TACoPc (1:8) protonation* ↕ *5.31 eV* *β-TACoPc (1:8) protonation*
	β-TACoPc			

The stabilized structures in the DFT calculation reveal that the pristine *α*-TACoPc possesses intramolecular hydrogen bonding between the $–NH_2$ group and imine N at the meso-position of the Pc ring, with the former as the H-bond donor and the latter as the H-bond acceptor (Figure S5a). This H-bonding has a characteristic distance of 2.225 Å with an N-H---N bond angle of 129.75° (Table S1). This intramolecular hydrogen bond is thus moderate in strength and mostly electrostatic in nature.[22,23] Furthermore, the pristine *α* isomer lies at 0.87 eV (relative energy difference) lower than the corresponding *β* isomer on the potential energy surface, indicating that this type of H-bonding stabilizes the former (Table S1, and Figures S5a and S5b). However, such intramolecular hydrogen bonding is absent in the pristine *β* isomer

molecule, perhaps due to a lack of interaction between the H-bonding groups given their relatively large spatial separation. In essence, isomerism of the $-NH_2$ functionality in the N_4 macrocycle triggers non-covalent interactions in the α isomer, which is absent in the corresponding β isomer due to the large spatial separations of H-bonding groups (Figures S5a and S5b). Certain observations relating to structural geometry became apparent when DFT calculations were performed in the presence of protons (Figures S5c-S5f and Figures 1a and 1b), and these were deemed as relevant since we carried out charge storage investigations in proton-containing media (as discussed below). The β isomer displayed fairly stable structures when the molecule to proton ratio was 1:4, as well as 1:8, suggesting the possibility that all of the N atoms (8 N atoms) in the molecule had been protonated (Figures S5d, S5f and Figure 1b). However, the α isomer, which showed a stable structure when the molecule to proton ratio was 1:4, became highly unstable at a 1:8 molecule to proton ratio, suggesting that the protonation of eight N atoms, as in the case of β isomer, is highly unfavorable (Figures S5c, S5e and Figure 1a). DFT calculations also revealed that intramolecular H-bonding in the pristine α isomer grew stronger with a 1:4 molecule to proton ratio, as shown in Figure 1c and Figures S5a and S5c. The relative energy diagram (Figure 1c) shows that in the α isomer, the proton shuttles between amine nitrogen and imine nitrogen, which in turn stabilizes the structure by nearly 6 eV. This could explain the preferential protonation of imine N compared to amine N, with the consequence of the former being the H-bond donor and the latter being H-bond acceptor. DFT calculations show that this stability attained by the α isomer via intramolecular H-bonding will be lost upon further protonation at a 1:8 molecule to proton ratio due to structural deformation (Figure 1a, and Figure S5e). Therefore, DFT calculations indicate that the presence of intramolecular H-bonding in the α isomer restricts the extent of protonation of the N atoms, and that the absence of it in the β isomer allows the majority of its N atoms to be protonated. As we show below, this has important consequences in determining the EDL's structure and electrochemical capacity.

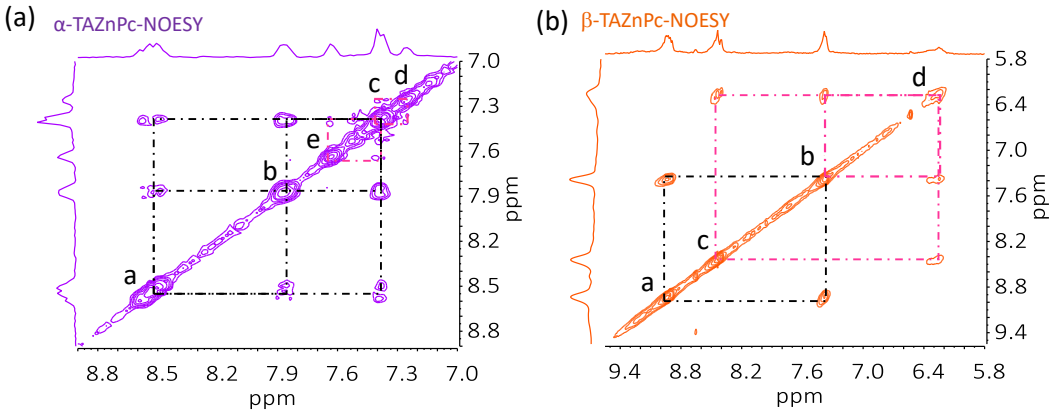

Figure S6 | 2D (^{1}H-^{1}H) NMR spectra (NOESY) of *α*-TAZnPc and *β*-TAZnPc isomeric molecules in DMSO-d$_6$. (a) NOESY spectra of *α*-TAZnPc and (b) NOESY spectra of *β*-TAZnPc.

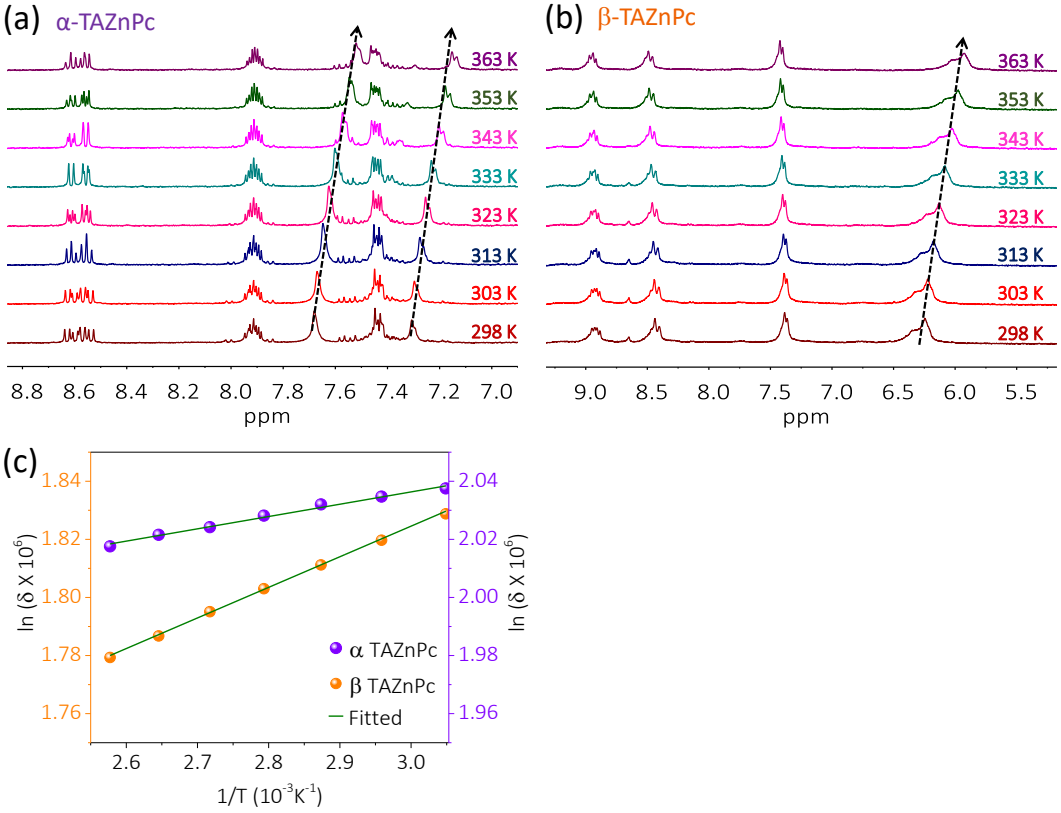

Figure S7 | ^{1}H NMR of variant temperature analysis in DMSO-d$_6$. Temperature-dependent (25^o to 90^o C) ^{1}H NMR spectra of (a) *α*-TNZnPc, (b) *β*-TNZnPc and (c) Arrhenius plot of chemical shift vs. inverse of temperature (T) for the amine protons in isomeric *α* and *β*-TAZnPc molecules extracted from their respective temperature-dependent ^{1}H NMR spectra.

1D NMR shows two distinct chemically shifted amine protons in the case of the *α* isomer (labelled as 'e' and 'd' in the inset of Figure 2a for *α*-TAZnPc), which could be

exchanged upon the addition of D_2O, thereby confirming their origin as being from amine protons (Figure 2a). This suggests that the chemical environments of amine protons in the α isomer are distinctly different, which is possible if there are intramolecular hydrogen bonding interactions involving the primary amine group and imine nitrogen in the Pc ring (as shown in the inset of Figure 2a). The corresponding NOESY 2D NMR suggest that the amine protons are in hydrogen bonding with imine nitrogen (Figure S6a). 1D NMR of the corresponding β isomer revealed only a broad amine proton signal (labelled as 'd' in the inset of Figure 2a for β-TAZnPc), which disappeared upon D_2O addition, suggesting that such intramolecular hydrogen bonding interactions are absent in the β isomer (Figure 2a). The corresponding NOESY 2D NMR further rule out these intramolecular hydrogen bonding interactions in the β isomer (Figure S6b), probably due to the unfavorable position of the H-bonding groups. Temperature-dependent NMR suggest a lower chemical shift slope for the amine protons in the α isomer, as compared to a noticeably higher slope for the amine protons in the β isomer (Figure S7). It should be noted that the chemical shift with respect to temperature for the amine protons in the α isomer is of the order expected for intramolecularly H-bonded protons, as reported in the literature.[24,25] All these favour the theoretical predictions by DFT, and suggest that the α isomer has intramolecular hydrogen bonding involving imine nitrogen and amine protons, as shown in Scheme S1.

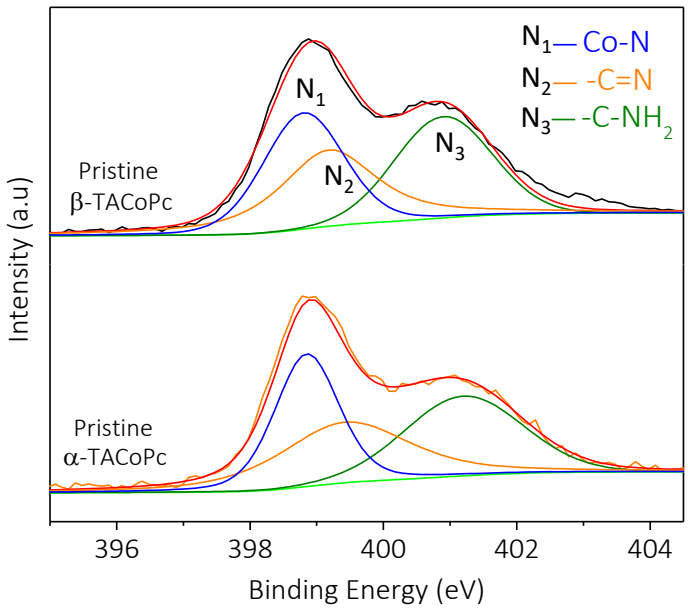

Figure S8 | XPS analysis. $N1_S$ XPS spectra for pristine α-TACoPc and β-TACoPc isomeric molecules.

Table S2 | Binding energy values. N1s binding energy values for α-TACoPc and β-TACoPc isomeric molecules (extracted from Figure 2b, 2c and Figure S8). N_1 (Co-N), N_2 (C=N, imine), N_3 (C-NH_2, amine) marked in Figure 2a).

Molecules	***α-TACoPc***			***β-TACoPc***		
	N_1	***N_2***	***N_3***	***N_1***	***N_2***	***N_3***
Pristine (eV)	*398.9*	*399.4*	*401.2*	*398.8*	*399.2*	*400.9*
Protonated (eV)	*399.1*	*400.8*	*401.7*	*399.2*	*400.9*	*401.9*
ΔB.E [Protonated - Pristine] (eV)	*0.2*	*1.4*	*0.5*	*0.4*	*1.7*	*1.0*
ΔB.E [Pristine α-TACoPc – Pristine β-TACoPc] (eV)	***N_1***		***N_2***		***N_3***	
	0.1		*0.2*		*0.3*	

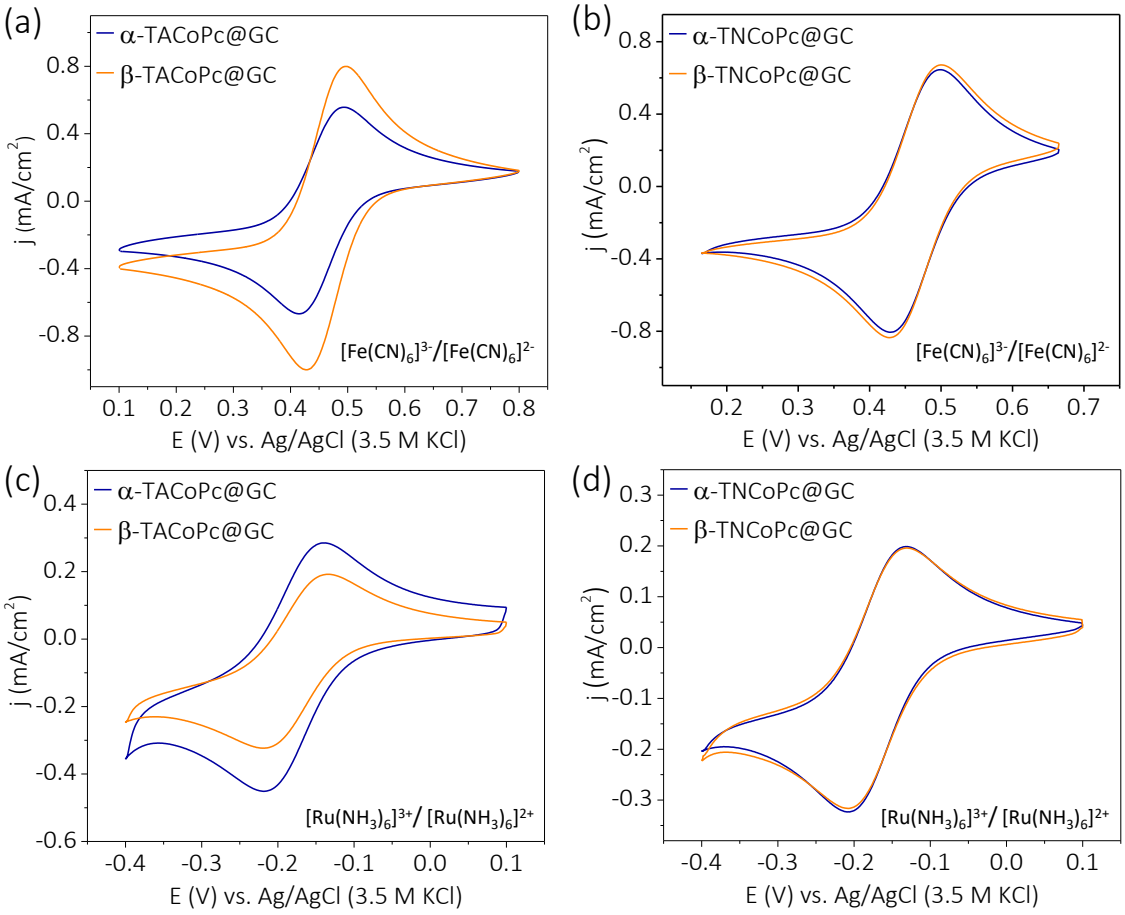

Figure S9 | Outer-sphere redox probe analysis. Cyclic voltammograms at a scan rate of 20 mV/s for *α*-TACoPc, *α*-TNCoPc, *β*-TACoPc and *β*-TNCoPc modified glassy carbon electrodes in N_2 saturated 0.5 M H_2SO_4 containing (a and b) 5 mM $[Fe(CN)_6]^{3-}$ and (c and d) 2 mM $[Ru(NH_3)_6]^{3+}$. (a and c) for *α*-TACoPc, and *β*-TACoPc and (b and d) for *α*-TNCoPc and *β*-TNCoPc modified glassy carbon (GC) electrodes.

It should be noted that if the double layer effect is indeed significant, a noticeable change in peak-to-peak separation is expected, however this is not observed in the present case. This is mainly because, both the isomeric molecules are exerting an attractive field (since proton charge assemblies are present in both molecules) on the ferricyanide species. Hence, the electrostatic current contribution is always parallel to the diffusion current in both the isomeric molecules. When the electrostatic current contribution is opposite to diffusion current, an opposite effect is expected which is evident in the case of $Ru(NH_3)_6^{2+/3+}$ complex. An alteration in peak-to-peak separation can be expected if one molecule exerts a repulsive field on the ferricyanide and the other molecule exerts an attractive field. Since, both the isomeric molecules exerts a field which is either attractive or repulsive, with a difference only in their magnitude, only an alteration in their electrostatic current contribution can be expected.

An investigation of the surface charge with charged outer-sphere redox probes, such as $[Fe(CN)_6]^{3-}$ and $[Ru(NH_3)_6]^{3+}$ (Figures S9a to S9d), suggests that in an acidic medium the β isomer can electrostatically attract negatively charged $[Fe(CN)_6]^{3-}$ and partially block positively charged $[Ru(NH_3)_6]^{3+}$, as compared to the α isomer (Figures S9a and S9c). This signals that, in an acidic medium, the β isomer acquires more positive charge density than the α isomer, which is a direct consequence of intramolecular hydrogen bonding in the latter (as explained above). Detailed explanations are provided in page S19 of SI and Figure S9.

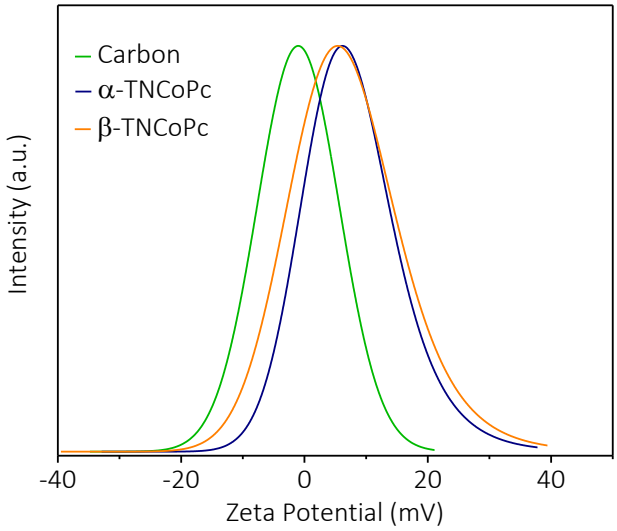

Figure S10 | Zeta potential analysis. Zeta potential profile of carbon, α-TNCoPc and β-TNCoPc isomeric molecules in proton containing medium.

The experimental observations with outersphere redox probes are directly supported by the zeta-potential measurements of structural isomers of amino molecules in a proton-containing medium, wherein the β isomer demonstrated a significantly positive (~14.5 mV) Zeta potential as compared to the corresponding α isomer (~4 mV) and carbon (~-1 mV), respectively (Figure 2d).

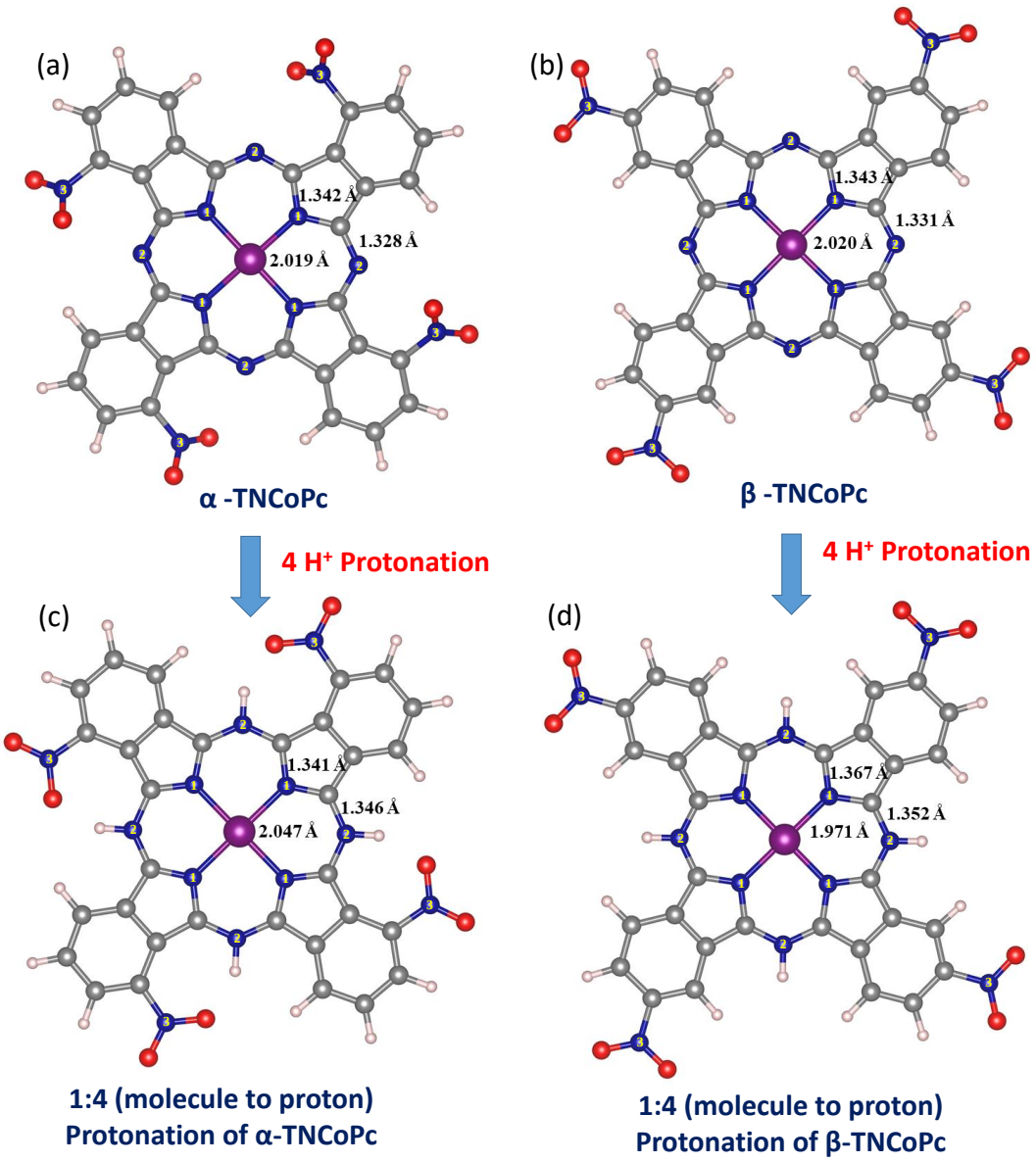

Figure S11 | DFT analysis of –NO_2 isomeric molecules. Stable geometry of pristine (a) *α*-TNCoPc and (b) *β*-TNCoPc isomers. Stable geometry of protonated (c) *α*-TNCoPc and (d) *β*-TNCoPc isomers with molecule to proton ratio of 1:4. (Nitrogen atoms are labeled in their stable geometry in Figure S11: N1: pyrrole nitrogen atoms; N2: iminic nitrogen atoms; and N3: nitrogen atom of NO_2 groups).

6. Assembly of α-TAMPc and β-TAMPc on glassy carbon (GC) electrodes (Metal:- *Co, Ni, Cu, Zn*)

Assembly of α and β-TAMPc molecules were achieved by the self-assembly process. 6 mM α and β-TAMPc solutions were prepared in dimethylformamide (DMF) by ultrasonication. GC electrodes were first polished by alumina polishing powder and then cleaned electrochemically. The polished GC electrode was electrochemically cleaned between the potential 0.2 to 1.3 V vs. RHE in 0.5 M H_2SO_4 using potentiodynamic cycling until reproducible voltammograms were obtained. The electrodes were washed with a copious amount of distilled water and finally with DMF and the electrode were then incubated respective phthalocyanine solution for ~6 hours. The modified electrodes were washed with fresh DMF to remove physisorbed molecules and finally washed with distilled water.

7. Molecular surface coverage analysis: quartz crystal microbalance (QCM) study

To understand the pristine behavior of the isomeric molecules, the electrochemical experiments were also carried out by forming a monolayer of α-TACoPc isomer and β-TACoPc isomer on glassy carbon electrodes. The formation and surface coverage of monolayer was confirmed by the Quartz Crystal Microbalance (QCM) studies. Quartz Crystal Microbalance (QCM) measurements were carried out in flow cell mode using a carbon coated quartz resonator (9.12 MHz) as the base crystal. A 0.2 mM molecular catalyst solution in DMF was circulated at a flow rate of 1 ml/min. Initially, the DMF solution was circulated for 2 hours to get a stable background signal. This was followed by passing the isomeric molecule solution for ~6 hours to allow the formation of a monolayer on the crystal. Finally, the fresh DMF solution was again passed to remove any weakly adsorbed molecular catalyst.

The Sauerbrey equation was then used to find the mass of adsorbed molecules on the crystal by correlating the frequency shift (Δf) to mass change (Δm) as in equation S2.[26-28]

$$\Delta m = -c\left(\frac{\Delta f}{n}\right) \ldots\ldots \text{(S2)}$$

where, Δf is the net resonance frequency shift due to adsorption of molecules and n is the overtone number (QCM analysis were measured at the third overtone (n=3)). The sensitivity (c) of the QCM crystal was 5.608 ng cm^{-2} Hz^{-1}.

The surface coverage (Γ, $mol.cm^{-2}$) was calculated using equation S3,

$$\Gamma = \frac{\Delta m}{Molecular\ mass} \ldots\ldots \text{(S3)}$$

The surface coverage values were $4.67 \cdot 10^{-11}$ mol/cm^2 and $4.73 \cdot 10^{-11}$ mol/cm^2 for α-TACoPc and β-TACoPc isomeric molecules, respectively (Figure S12, and Table S3). These values are lower than the theoretically expected value of $1.1.10^{-10}$ mol/cm^2 for a perfectly flat phthalocyanine monolayer on an electrode surface, signifying the adsorption of isomeric molecules as a monolayer with an almost flat orientation on the electrode surface.[5,6,29]

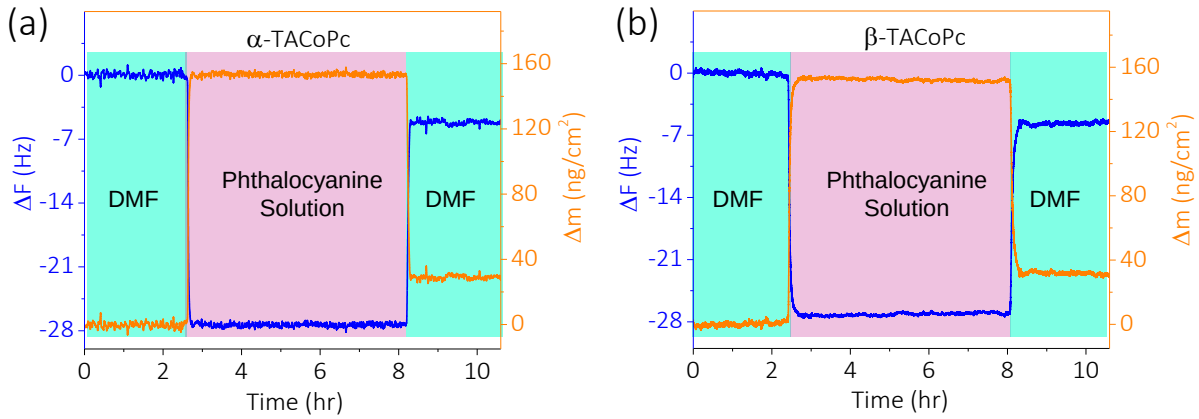

Figure S12 | Molecular surface coverage analysis. Quartz crystal microbalance (QCM) response during the adsorption of isomeric molecules (α-TACoPc and β-TACoPc) on a carbon coated quartz resonator from 0.2 mM solution of (a) α-TACoPc and (b) β-TACoPc in dimethylformamide (DMF). The blue trace shows the frequency change during the adsorption and the orange trace shows the calculated mass change using the Saurbrey equation.

Table S3 | Surface coverage (Γ) in mol/cm^2 for α-TACoPc and β-TACoPc isomeric molecules (extracted from Figure S12).

Electrode	***Surface Coverage (Γ)***
α-TACoPc@GC	$4.67.10^{-11}$ *mol/cm^2*
β-TACoPc@GC	$4.73.10^{-11}$ *mol/cm^2*

8. Fundamental Understanding of Electrochemical Properties of Molecules

a. Specific capacitance (C_{sp}) calculations for monolayer electrode.

The specific capacitance or capacitance/cm^2 was calculated from cyclic voltammetry (CV) curves (in three electrode configurations) at various scan rates using the following equation S4. [30-32]

$$C_{sp} = \frac{\int i \times dV}{2 \times A \times \nu \times \Delta V} \ldots\ldots (S4)$$

where, C_{sp} is specific capacitance (F/cm^2), $\int i.dV$ is the integrated area in the cyclic voltammogram, A is geometrical area of the electrode (cm^2), ν is the scan rate (mVs^{-1}), and ΔV is the potential window (V).

The C_{sp} from the galvanostatic charge-discharge (GCD) measurements (in three electrode configurations) was calculated using the equation (S5)

$$C_{sp} = \frac{I \times \Delta t}{A \times \Delta V} \ldots\ldots (S5)$$

where C_{sp} is specific capacitance (F/cm^2), I is applied current (A), ΔV represents the potential window (V), Δt signifies discharge time (s), and A is geometrical area of the electrode (cm^2).

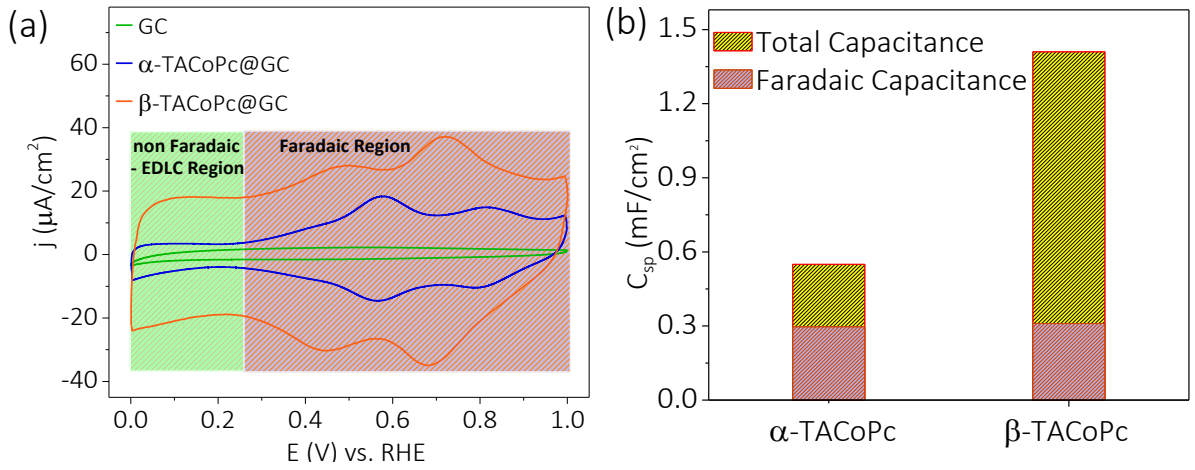

Figure S13 | Cyclic voltammetry (CV) analysis of monolayer modified electrodes and Faradaic contribution analysis. (a) Cyclic voltammograms of *α*-TACoPc and *β*-TACoPc isomeric molecules when incorporated as a monolayer on a glassy carbon electrode at a scan rate of 20 mV/s in N_2 saturated 0.5 M H_2SO_4. (b) Comparative bar diagrams depicting the Faradaic contribution to the overall capacitance of isomeric molecules when they are adsorbed as a monolayer on a glassy carbon electrode. Faradaic contributions are extracted from Figure R1 by integrating the charge under the redox peaks.

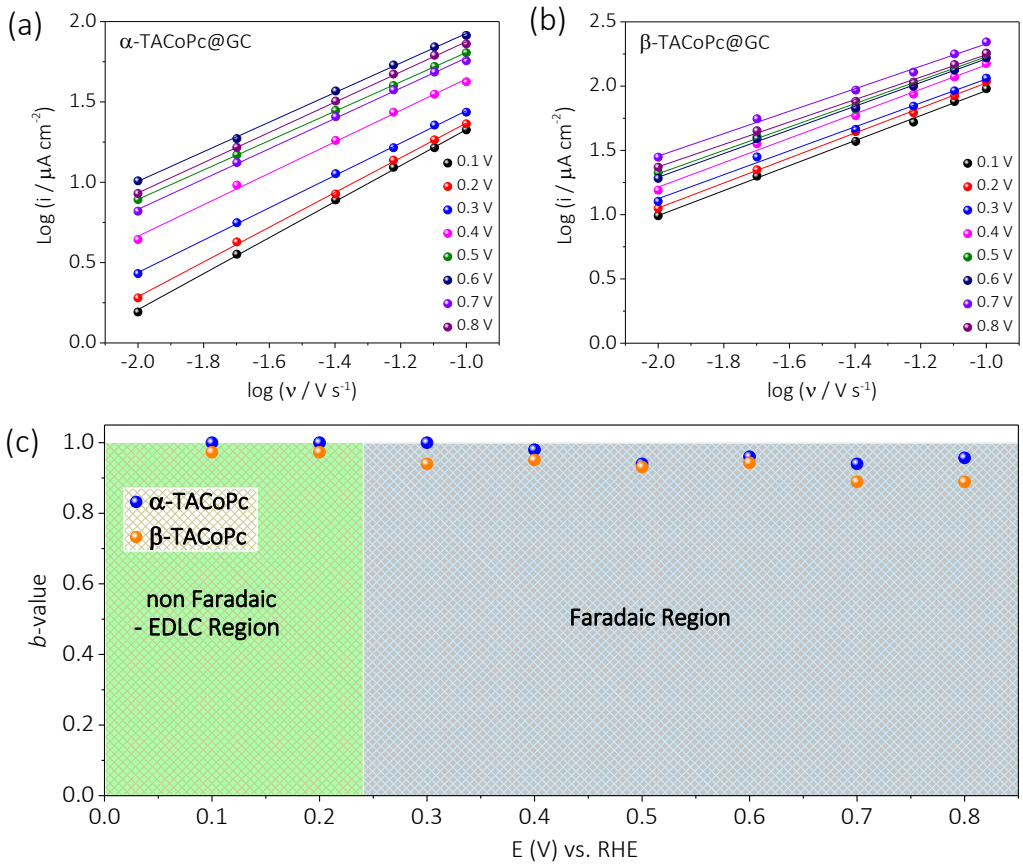

Figure S14 | Logarithmic relationship between currents and scan rates. Logarithmic relationship between currents obtained from the cyclic voltammograms and scan rates for (a) *α*-TACoPc and (b) *β*-TACoPc isomeric molecules when they are incorporated as a monolayer on a glassy carbon electrode. (c) The calculated *b* values for the *α*-TACoPc and *β*-TACoPc isomeric molecules at different potentials. The *b* values are extracted from Figure R2a and R2b by calculating the slope values.

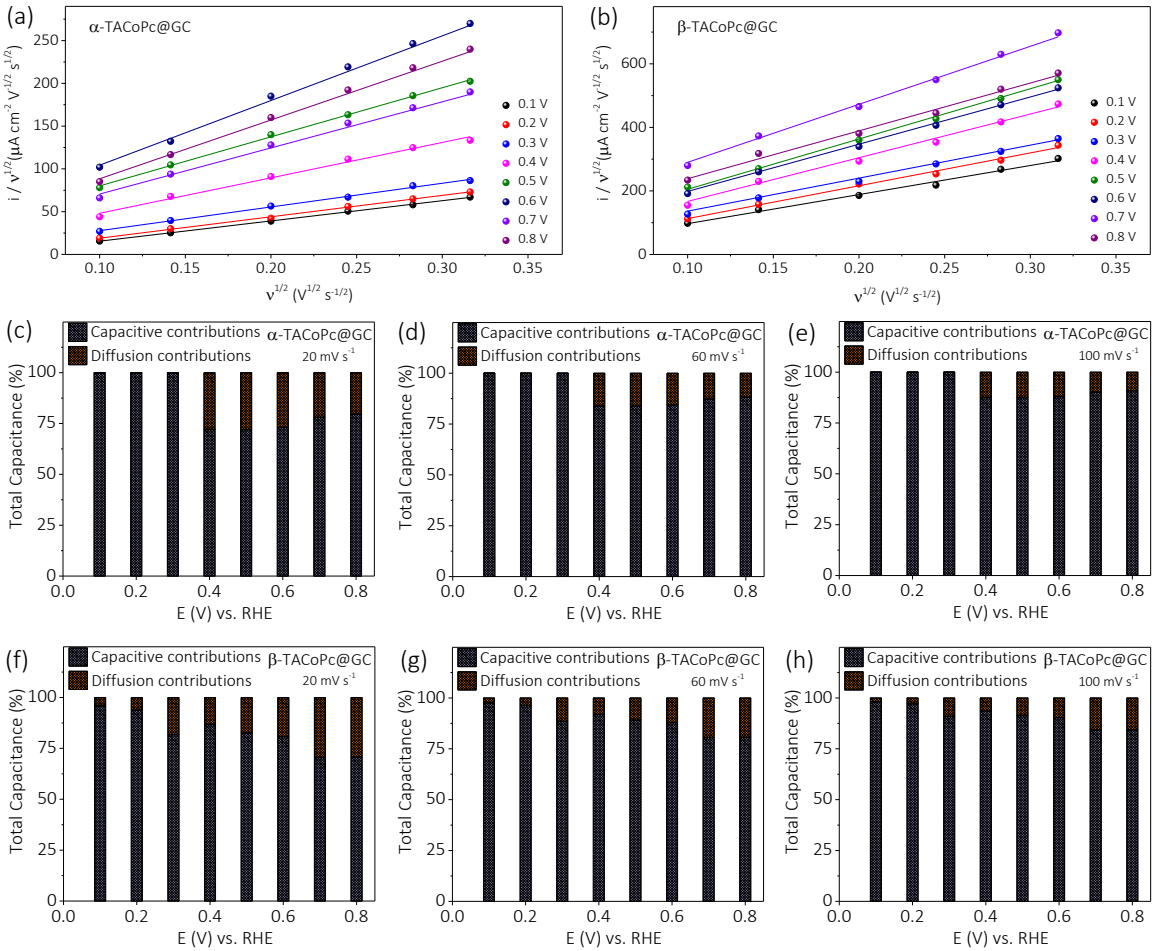

Figure S15 | Capacitive contributions analysis: Plot of $i/\nu^{1/2}$ vs. $\nu^{1/2}$ for α-TACoPc and (b) β-TACoPc isomeric molecules. Histogram plot shows the percentage of capacitive and diffusion contributions at 20 mV/s, 60 mV/s and 100 mV/s scan rates for (c-e) α-TACoPc and (f-h) β-TACoPc isomer molecules. The capacitive currents (blues shaded regions) and diffusion currents (orange shaded regions) are determined from the total current using equation S6.

A closer examination of the voltammetric sweep rate dependence enables one to distinguish quantitatively the capacitive contribution to the current response. The current response at different potentials is expressed as being the combination of two separate mechanisms, surface capacitive effects and diffusion-controlled processes,[33] equation S6. These capacitive effects were characterized by analyzing the cyclic voltammetry data at various sweep rates.

$$i\,(V) = k_1\nu + k_2\nu^{1/2} \ldots\ldots \text{(S6)}$$

In equation S6, $k_1\nu$ and $k_2\nu^{1/2}$ correspond to the current contributions from the surface capacitive effects and the diffusion-controlled process, respectively. Thus, by determining k_1 and k_2, it is possible to quantify, the current fraction arising out of these contributions. Figure S15c-e and S15f-h show the total stored capacitance and the relative contributions associated

with both diffusion (grey shaded area) and capacitive processes (blue shaded area) in α-isomer and β-isomer molecules. Further, histogram plot shows the decoupling of current contributions at 20 mV/s, 60 mV/s and 100 mV/s scan rate, respectively, Figure S15c-h.

Taken together, the capacitive contribution dominates the charge storage mechanism especially in the EDL region, and its contribution to the overall scales up with respect to the scan rate.

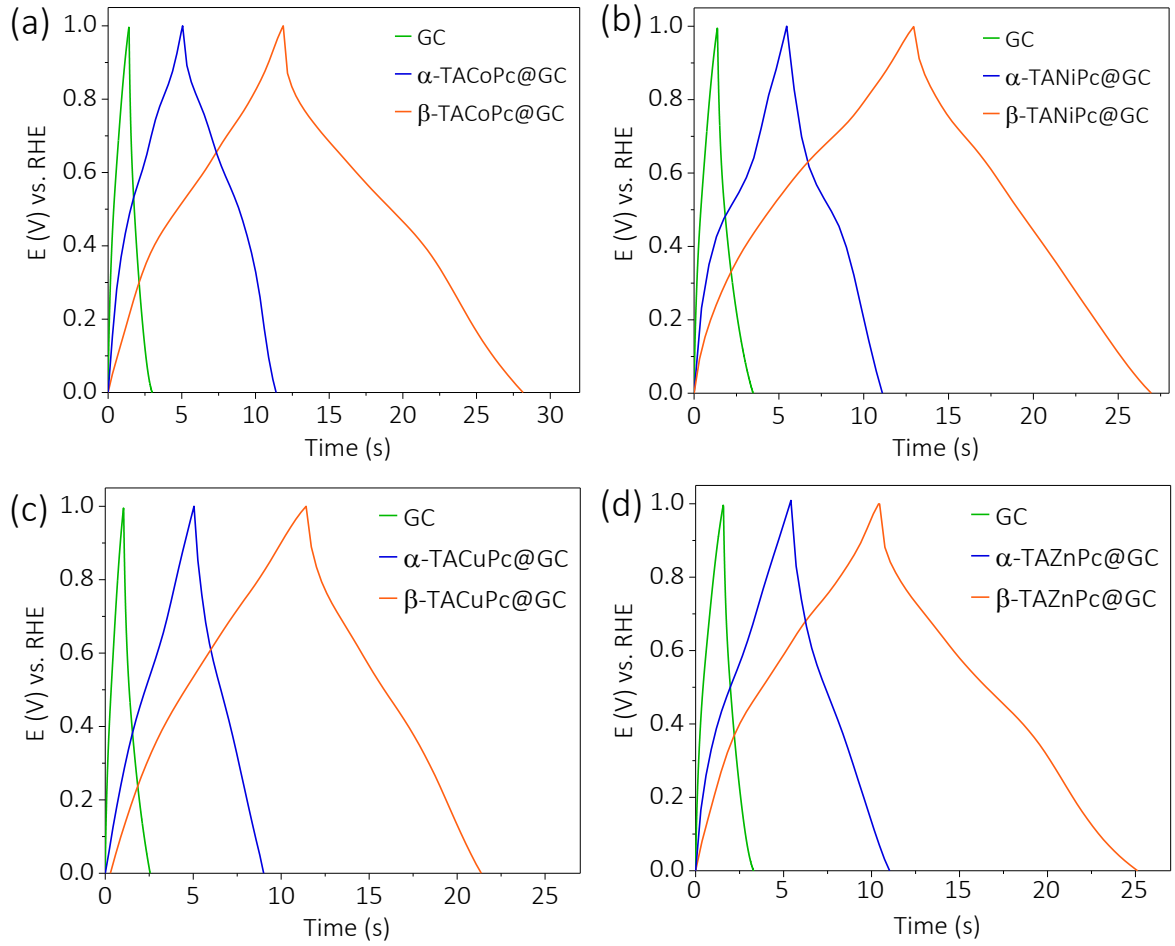

Figure S16 | Galvanostatic charge-discharge analysis. Galvanostatic charge-discharge at a rate of 0.1 mA/ cm^2 in N_2 saturated 0.5 M H_2SO_4 for (a) α-TACoPc and β-TACoPc, (b) α-TANiPc and β-TANiPc, (c) α-TACuPc and β-TACuPc and (d) α-TAZnPc and β-TAZnPc isomeric molecules when they are adsorbed as a monolayer on a glassy carbon (GC) electrode.

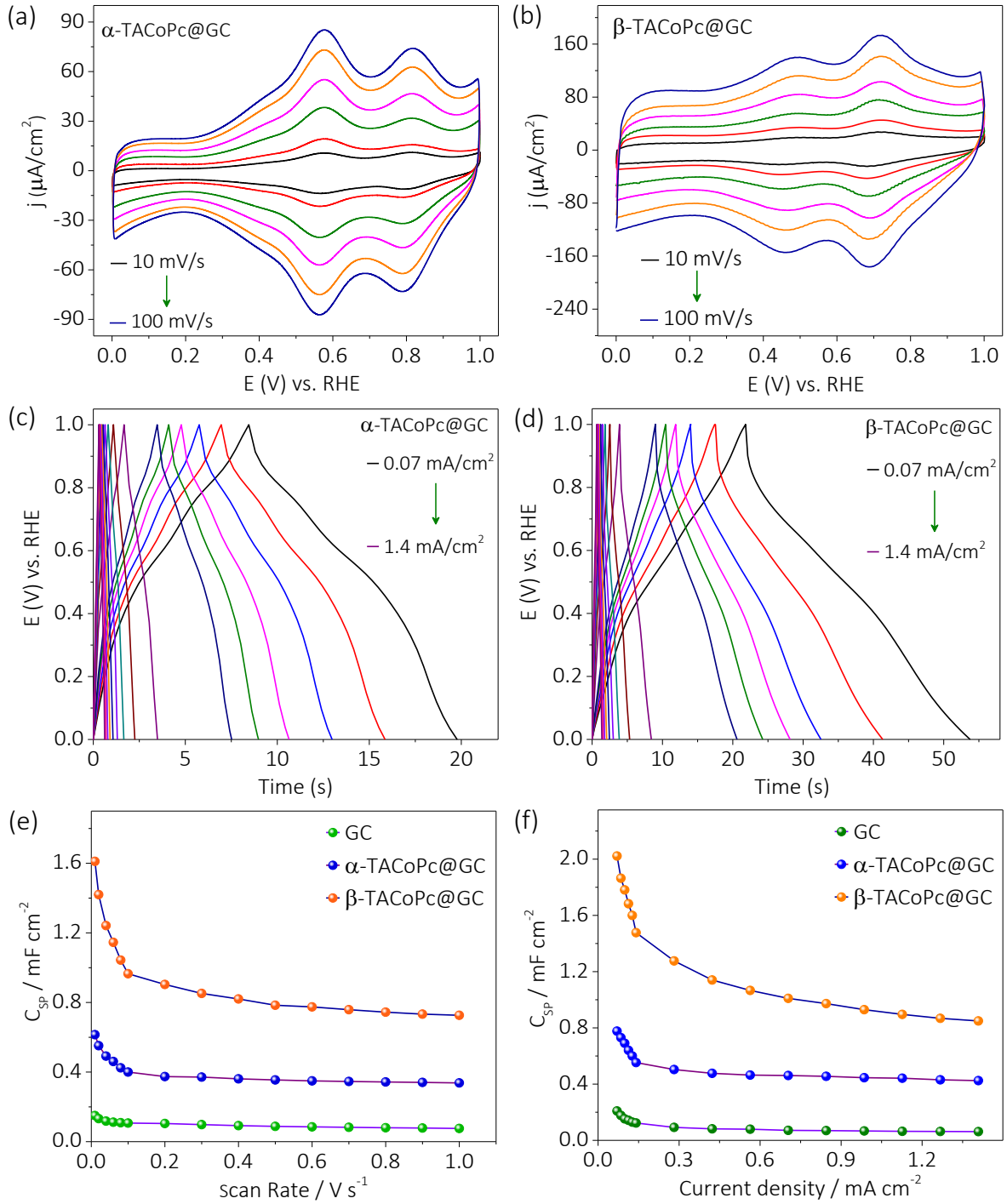

Figure S17 | Rate capability analysis. Rate profiles for *α*-TACoPc and *β*-TACoPc isomeric molecules when they are adsorbed as a monolayer on a glassy carbon electrode surface. (a, b) Cyclic voltammetry, (c, d) galvanostatic charge-discharge, (e) rate profiles from cyclic voltammetry and (f) rate profiles from galvanostatic charge-discharge. Specific capacitance (F/cm^2) values were calculated based on the geometric area of the electrode.

Table S4 | Comparative performance metrics with different metal ions. Supercapacitive properties of α-TAMPc and β-TAMPc electrodes (M – Co, Ni, Cu and Zn). Parameter are extracted from Figure 3 and Figure S16.

Types of central metal ions	***From Cyclic Voltammetry C_{sp} (mF/cm^2)***			***From Galvanostatic Charge-Discharge C_{sp} (mF/cm^2)***		
	α	***β***	***[β- α]***	***α***	***β***	***[β- α]***
Co	*0.55 (over all capcity)* *0.297 (Faradic contribution) 54%*	*1.41 (over all capcity)* *0.312 (Faradic contribution) 22%*	*0.86*	*0.64*	*1.67*	*1.03*
Ni	*0.49*	*1.30*	*0.81*	*0.55*	*1.48*	*0.93*
Cu	*0.52*	*1.34*	*0.82*	*0.57*	*1.51*	*0.94*
Zn	*0.54*	*1.35*	*0.81*	*0.58*	*1.50*	*0.92*

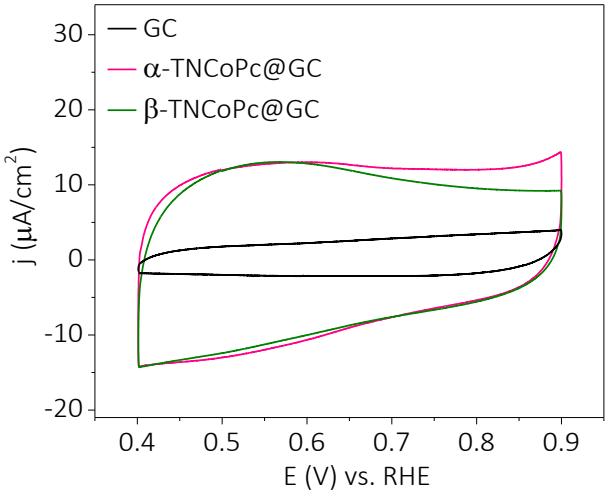

Figure S18 | Cyclic voltammetry of the cobalt based –NO_2 isomeric molecules. Cyclic voltammograms at a scan rate of 20 mV/s for α-TNCoPc and β-TNCoPc isomeric molecules (adsorbed as a monolayer on a glassy carbon (GC) electrode) in N_2 saturated 0.5 M H_2SO_4 solutions.

9. Synthesis and characterization of α-TACoPc and β-TACoPc anchored on YP-50F

The TACoPc@YP-50F hybrid was prepared by TACoPc with activated carbon YP-50F in N, N-dimethyl formamide (DMF) with the assistance of sonication and magnetic stirring. The YP-50F was purchased from Kuraray chemicals. We have optimized the weight ratio of TACoPc in YP-50F from the specific capacitance obtained from cyclic voltammetry and galvanostatic charge discharge methods. Weight ratios of 2:1 (YP50F (nearly 67%) and TACoPc (nearly 33%)), 4:1 (YP50F (nearly 80%) and TACoPc (nearly 20%)) and 1:1 (YP50F (nearly 50%) and TACoPc (nearly 50%)) were used for optimization studies. Since 2:1 ratio resulted in higher capacitance over the other weight ratios, the weight ratio of isomeric molecules on YP50F was maintained at 2:1 (YP50F (nearly 67%) and TACoPc (nearly 33%)) for comparative purposes. The TACoPc isomers and YP-50F were dispersed in DMF followed by 30 min of sonication to obtain a well-mixed suspension. The mixed suspension was further stirred at 80^{o}C temperature for 24 h. Subsequently, the mixture was centrifuged and the precipitate was washed with DMF followed by ethanol several times. Finally, the precipitate was lyophilized to yield the final product.

The presence of phthalocyanine molecules on YP-50F is validated via FTIR, Raman spectroscopy and FESEM (Figures S19 and S20). Briefly, we found that: FTIR results display the features of TACoPc in TACoPc@YP-50F, along with corresponding YP-50 features (Figure S19a); Raman spectra show the presence of a characteristic defect and graphitic bands in YP-50F as well as in the composites (Figure S19b), although the phthalocyanine features were almost entirely masked by the intense YP-50F bands. Nevertheless, the I_D/I_G (intensity of defect band / intensity of graphitic band) ratio in YP-50F demonstrates a noticeable increase once anchored with the TACoPcs isomers, suggesting their successful incorporation.[33-35] Scanning electron microscopy (SEM) with energy dispersive X-ray spectroscopy (EDS), shown in Figure S20, indicate the characteristic spherical morphology of YP-50F, and the EDS spectra demonstrate the presence of Co, N and C, further confirming the successful incorporation of TACoPcs into the composite. Transmission electron microscopy (TEM) images, Figure S21, further support the incorporation of isomeric molecules onto YP-50F. The above findings thus serve to affirm the presence of YP-50F and TACoPcs isomers as part of the electrode architecture.

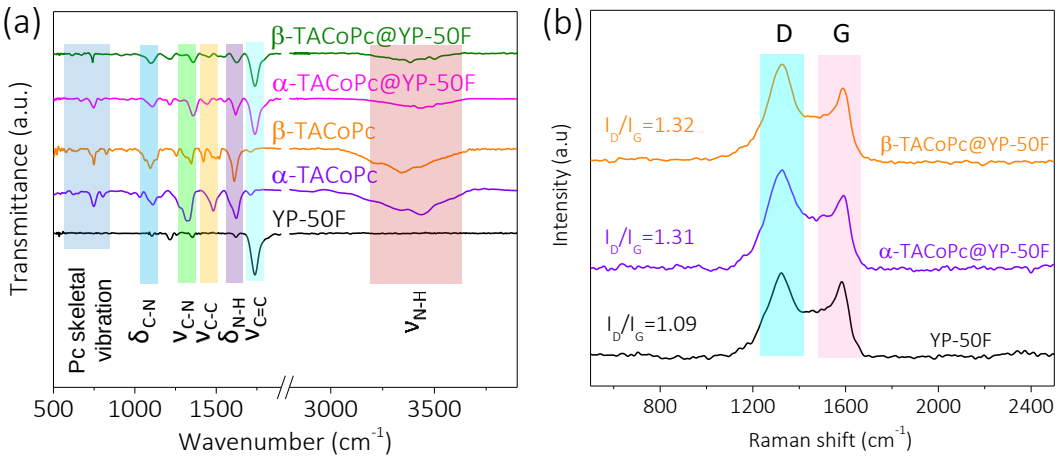

Figure S19 | (a) FTIR spectroscopy and (b) Raman spectroscopy of *α*-TACoPc@ YP-50F and *β*-TACoPc@ YP-50F.

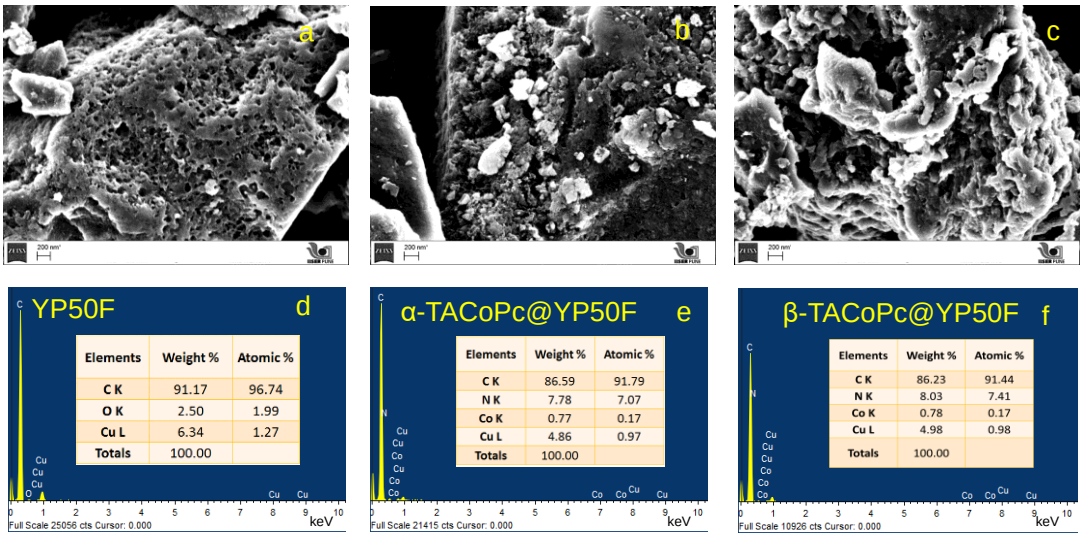

Figure S20 | FESEM images and EDS patterns of (a and d) YP-50F, (b and e) *α*-TACoPc@YP-50F (c and f) and *β*-TACoPc@YP-50F. (Cu signal in the EDS is derived from the Cu substrate).

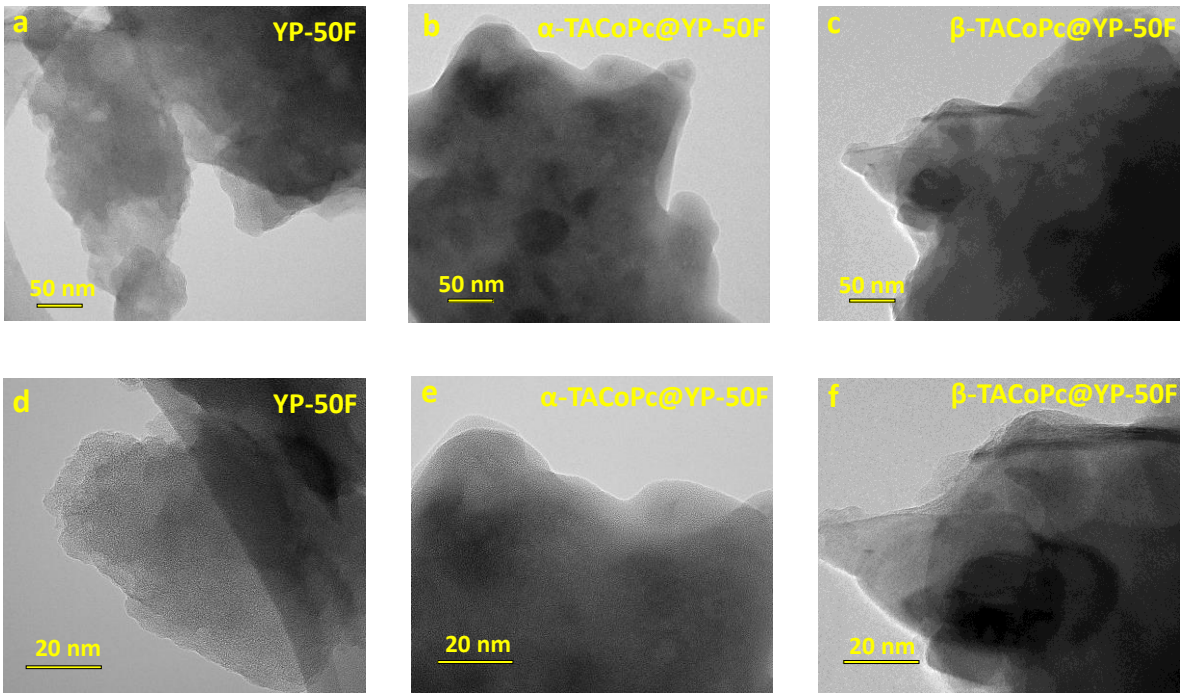

Figure S21 | TEM images of (a and d) YP-50F, (b and e) *α*-TACoPc@YP-50F and (c and f) *β*-TACoPc@YP-50F.

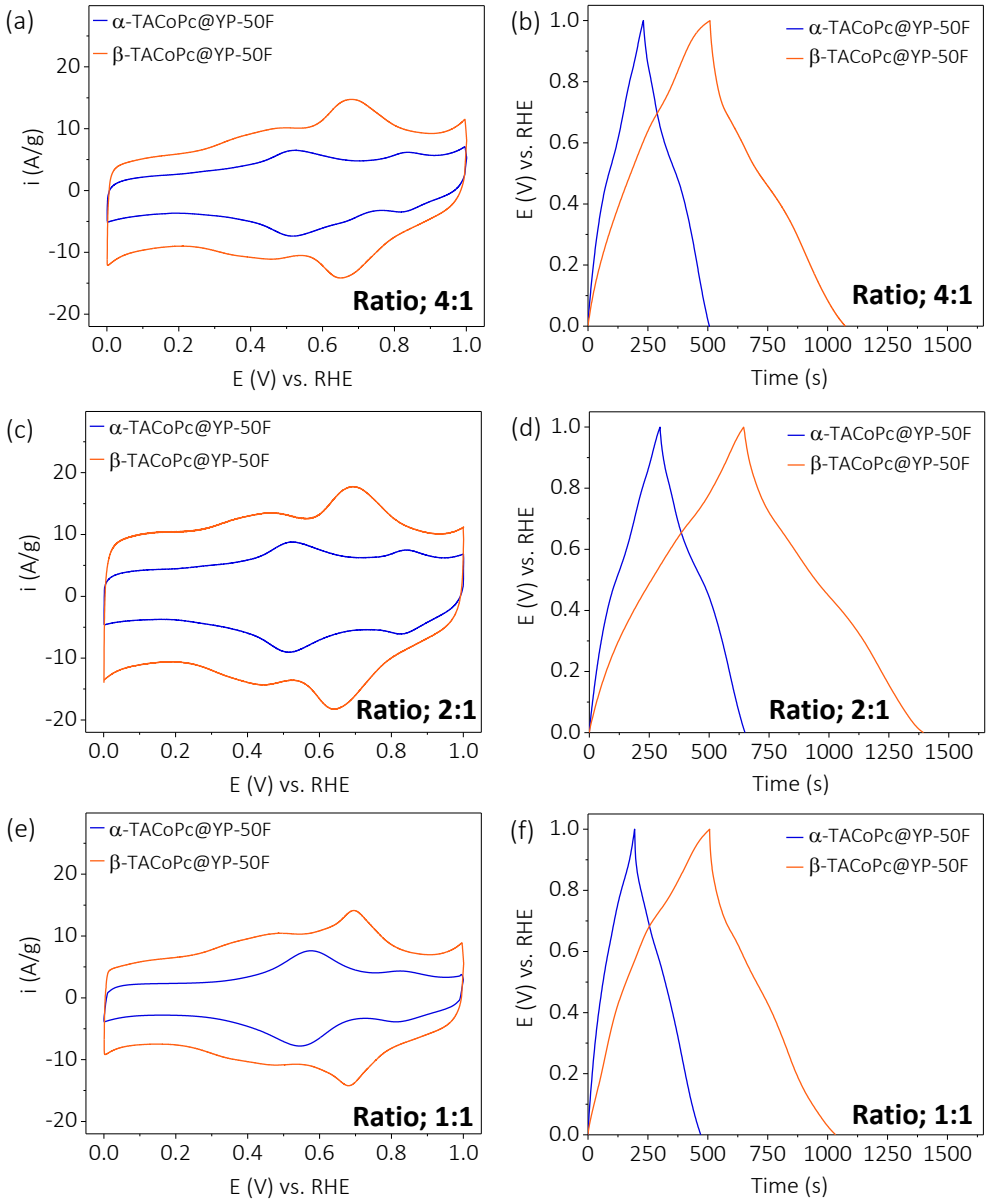

Figure S22 | Charge-discharge characteristics of different ratios of TACoPc isomers on YP-50F. (a, c and e) Cyclic voltammetry and galvanostatic charge-discharge profiles (b, d and f). (a and b) Correspond to 4:1 (YP-50F to TACoPc isomer) weight ratio, (c and d) stand for to 2:1 weight ratio and (e and f) represent the data for 1:1 weight ratio.

We have performed the charge-discharge measurements for different composite ratios (YP50F:TACoPc isomer) and the obtained results show that a weight ratio of nearly 2:1 resulted in higher specific capacitance compared to the other ratios of 4:1 and 1:1, Figure S20 and Table S5. Therefore, for comparative purposes, the weight ratio of α and β isomers on YP-50F was maintained at 2:1. The enhanced capacitance of 2:1 composite could be due to the

interplay between the overall electronic conductivity of the composite electrode and the number of isomeric molecules accessible to the electrolyte for the charge storage.

Table S5| Supercapacitive properties of YP-50F and its composites with different weight ratios of *α*-TACoPc and *β*-TACoPc isomers on YP-50F electrodes, determined from galvanostatic charge-discharge at 1 A/g and cyclic voltammograms at 5 mV/s scan rate. The parameters are extracted from Figure S22.

Ratio of composites (YP50F:TACoPc)	***From Cyclic Voltammetry C_{sp} (F/g)***		***From Galvanostatic Charge-Discharge C_{sp} (F/g)***	
	α-TACoPc	***β-TACoPc***	***α-TACoPc***	***β-TACoPc***
4:1	248	519	280	561
2:1	323	675	359	729
1:1	225	498	261	542

10. Electrochemical rate capability analysis in a 3-electrode configuration

a. Specific capacitance, energy density and power density calculations of molecular supercapacitor for three electrode configurations

The specific capacitance (C_{sp}) or capacitance/gram was calculated from cyclic voltammetry (CV) curves (in three electrode configurations) at various scan rates using the following equation S7.[30-32]

$$C_{sp} = \frac{\int i \times dV}{2 \times m \times \nu \times \Delta V} \ldots\ldots (S7)$$

where, C_{sp} is specific capacitance ($F.g^{-1}$), $\int i.dV$ is the integrated area in the cyclic voltammogram, m is mass of the active material (g) or , ν is the scan rate (mVs^{-1}), and ΔV is the potential window (V).

The C_{sp} from the galvanostatic charge-discharge (GCD) measurements (in three electrode configurations) was calculated using the equation (S8)

$$C_{sp} = \frac{I \times \Delta t}{m \times \Delta V} \ldots\ldots (S8)$$

where C_{sp} is specific capacitance ($F.g^{-1}$), I is applied current (A), ΔV represents the potential window (V), Δt signifies discharge time (s), and m is the mass of the active material (g).

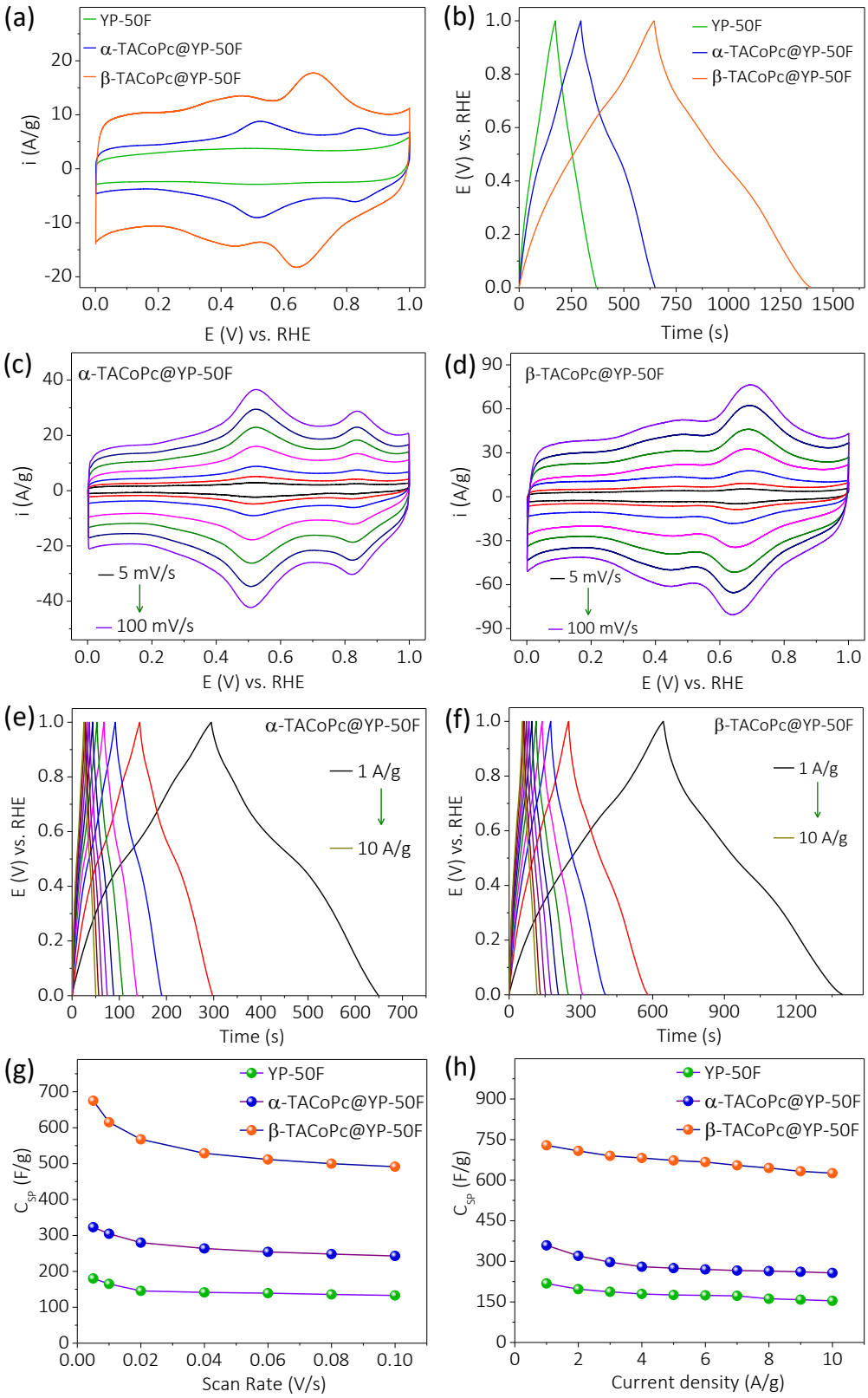

Figure S23 | Rate capability analysis. Charge-discharge characteristics of α-TACoPc@YP-50F and β-TACoPc@YP-50F. (a, c and d) Cyclic voltammetry, (b, e and f) galvanostatic charge-discharge profiles, (g) rate profiles from cyclic voltammetry and (h) rate profiles from cyclic voltammetry.

Table S6 | Comparison of performance metrics of SCs. Supercapacitive properties of YP-50F and its composites with α-TACoPc and β-TACoPc electrodes determined using the galvanostatic charge-discharge at 1 A/g and voltammograms of 5 mV/s scan rate.

Electrodes	***From Cyclic Voltammetry C_{sp} (F/g)***	***From Galvanostatic Charge-Discharge C_{sp} (F/g)***
YP-50F	180	217
α-TACoPc	323	359
β-TACoPc	675	729

11. Supercapacitor performance of two electrode configuration

a. Cell fabrications

Two-electrode cells consisted of *α*/*β*-TACoPc@YP-50F electrode and counter electrode (AC), assembled into two electrodes split test cell (MTI Cooperation, USA). The *α*/*β*-TACoPc@YP-50F electrodes were fabricated as described on pages S28-29, using carbon paper (AvCarb MGL190) as the current collector.

b. *Counter electrode fabrication*

Activated Carbon (AC) counter electrode: The AC (YP-50F (Kuraray Chemical Company)) were used as received. A mixture of 95 wt.% AC and 5 wt.% of Nafion binder were manually mixed in IPA until a homogenous ink was obtained. The ink was coated into carbon paper sheets with a thickness of ~0.15 mm as supercapacitor electrodes (1.4 cm diameter), with mass loading of 6.5 mg/cm².

c. *α/β-TACoPc@YP-50F / AC two electrode split test cell*

Two-electrode split test cell were assembled according to established protocols.[37] Briefly, a circular *α*/*β*-TACoPc@YP-50F electrode (1.4 cm diameter) was fabricated as described on pages S29-S30. Mass loading was 3.25 mg/cm^2. The whole electrode assembly is shown below Figure S24a. This electrodes were stacked with a glass fiber filter paper separator (thickness = 0.20 mm) wet with 400 µL of 0.5 M H_2SO_4 aqueous electrolyte. The stack was enclosed in a split test cell and assembled with silicone O ring rubber to prevent electrolyte evaporation and short circuiting. The two electrode split test cell was then tested using a standard two electrode measurement clip, Figure S24b.

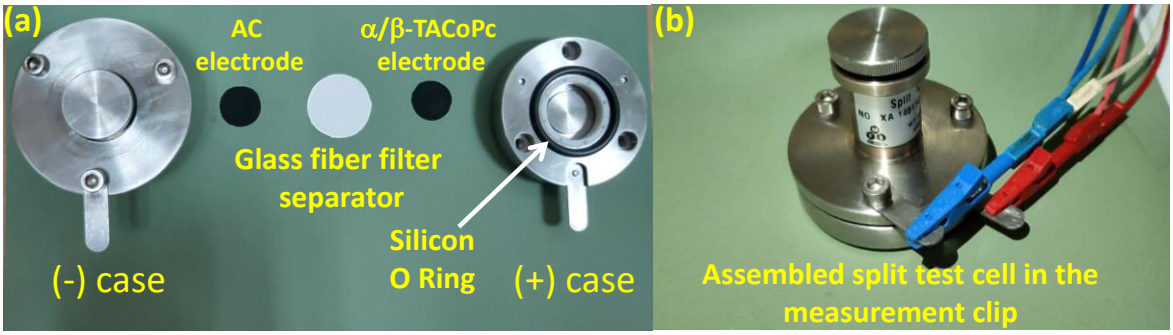

Figure S24 | Two electrode cell fabrication. Photographs showing (a) the components of a *α*/*β*-TACoPc@YP-50F / AC two electrode split test cell before assembly and (b) a split test cell in the measurement clips.

12. Calculation of specific capacity, specific energy and specific power for asymmetric two electrode configuration

The specific capacity, energy, and power for the two-electrode cells were calculated from galvanostatic charge discharge data (discharge cycle). The specific capacity was calculated using the equation S9,[38]

$$Q_s = \frac{i \times t}{m_c} \ldots\ldots\ldots \text{(S9)}$$

where *i* is the current, *t* is the discharge time, and m_c is the mass of active material (α/β-TACoPc@YP-50F) on the cathode. For calculating specific energy and power of the two-electrode cell, we use the total mass of cell components, as reported in the literature.[38,39] Specific energy is calculated using the equation (S10),

$$E_s = \frac{i \times t \times \Delta E}{m_{total}} \ldots\ldots \text{(S10)}$$

where ΔE is the potential window and m_{total} is given by

$$m_{total} = m_a + m_c \ldots\ldots \text{(S11)}$$

where m_a is the mass of AC required to balance the measured discharge Q or C, respectively.

Specific power was calculated using the equation (S12),

$$P_s = \frac{i \times \Delta E}{m_{total}} \ldots\ldots \text{(S12)}$$

13. Electrochemical performance in a two electrode configuration

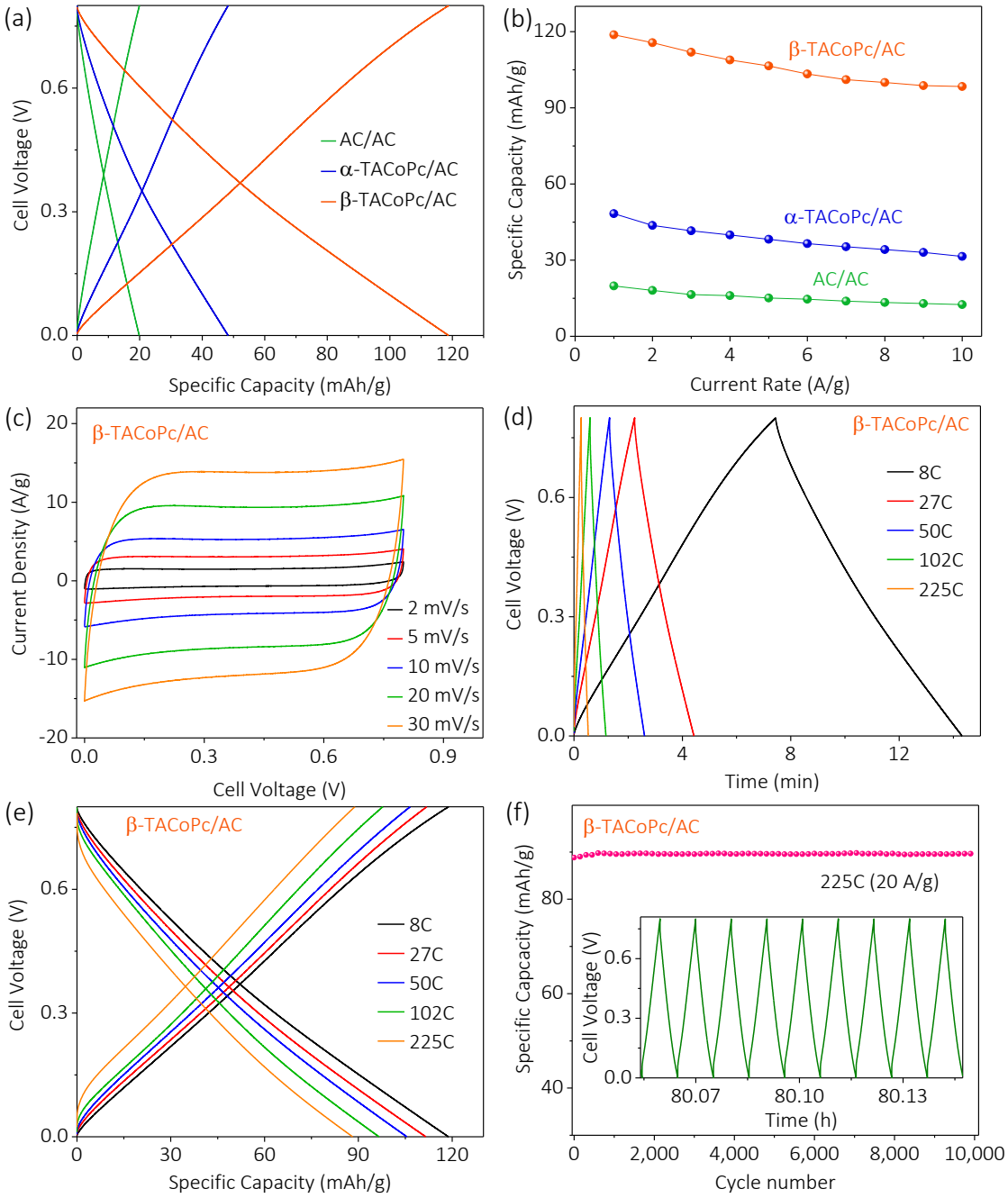

Figure S25 | Electrochemical performance in a two electrode configuration. Characterization of two-electrode split test cell assembled for *α*/*β*-TACoPc (+) electrodes and activated carbon (-) electrodes. (a) Galvanostatic charge-discharge (1 A/g) and (d) rate profiles. (c) Cyclic voltammetry profile for the *β*-TACoPc / AC cell at different rates, (d) galvanostatic charge-discharge characteristics of *β*-TACoPc / AC and (e) corresponding specific capacity profile. (f) Cycling performance of the *β*-TACoPc / AC split test cell at a rate of 225C (20 A/g), inset is a portion of the charge-discharge curves of the device obtained during the 4th day of repetitive cycling.

14. Summary of performance metrics

Table S7 | Comparison of performance metrics of SCs. Supercapacitive properties of YP-50F and its composites with α-TACoPc and β-TACoPc electrodes determined using the galvanostatic charge-discharge at 1 A/g.

Electrodes	*Specific Capacitance / F g^{-1}*	*Specific Capacity / mAh g^{-1}*	*Specific Energy / W h kg^{-1}*	*Specific Power / W kg^{-1}*
AC / AC	*90.5*	*20*	*9.3*	*466*
α-TACoPc / AC	*218*	*48.3*	*12.9*	*267*
β-TACoPc / AC	*535*	*119*	*19.5*	*160*

Table S8 | Performance metrics of the *β*-TACoPc / AC cell device at various rates. As described above, capacitance and capacity are calculated using only the mass of β-TACoPc@YP-50F, while energy and power are calculated using the total mass of cell components.

Current Density / A g^{-1}	*Equivalent C-rate*	*Specific Capacitance / F g^{-1}*	*Specific Capacity / mAh g^{-1}*	*Specific Energy / W h kg^{-1}*	*Specific Power / W kg^{-1}*
1	*8C*	*535*	*119*	*19.5*	*160*
2	*17C*	*513*	*114*	*18.2*	*320*
5	*50C*	*479*	*106*	*17*	*800*
10	*102C*	*443*	*98*	*15.7*	*1600*
30	*380C*	*360*	*80*	*12.7*	*4800*
50	*870C*	*259*	*58*	*9.2*	*8000*

15. Characteristic time constant (τ_0), self-discharge current (i_{sd}) and leakage current (i_{lk}) measurements

The characteristic time constant (τ_0) (also known as the relaxation time) reflects the minimum time required to discharge the capacitor fully[40-42] and it was estimated from the equation, S13.

$$\tau_0 = 1/f_o \quad \text{.....(S13)}$$

The characteristic frequency known as "knee" or "onset" frequency (f_o) which reflects the power capability of a supercapacitor, was calculated by plotting imaginary part of capacitance (C") as a function of frequency. The C" is associated with the energy loss and the real part (C') reflects the deliverable capacitance and these can be calculated according to the following equations S14 and S15.[41,43]

$$C''(\omega) = \frac{Z'(\omega)}{\omega |Z(\omega)|^2} \quad \text{..... (S14)}$$

$$C'(\omega) = \frac{-Z''(\omega)}{\omega |Z(\omega)|^2} \quad \text{..... (S15)}$$

where $|Z(\omega)|$ is the impedance modulus and $C''(\omega)$ and $C'(\omega)$ is imaginary and real parts of capacitance.

Self-discharge experiments were performed by measuring the time within which the voltage dropped from the completely charged state to the potential equal to mean of charged state and the open circuit voltage (OCV). Leakage current was calculated by holding the potential at full charge and the current required to maintain the fully charged state was measured over time.[44-46] Before self-discharge and leakage current measurements, initially, the system was charged with a rate of 1 $mA \cdot g^{-1}$ to 1.0 V and then held at this voltage for 4 hours. After a full charge, the system was allowed to undergo self-discharge for ~15 hrs while monitoring the open circuit voltage decay. The self-discharge currents were estimated from the equation S16.[45]

$$i_{sd} = C \times \frac{(V_1 - V_2)}{\Delta t} \quad \text{..... (S16)}$$

V_1- potential of charged state, V_2- mean potential between charged state and the open circuit voltage and Δt-time (in sec) taken to reach V_2.

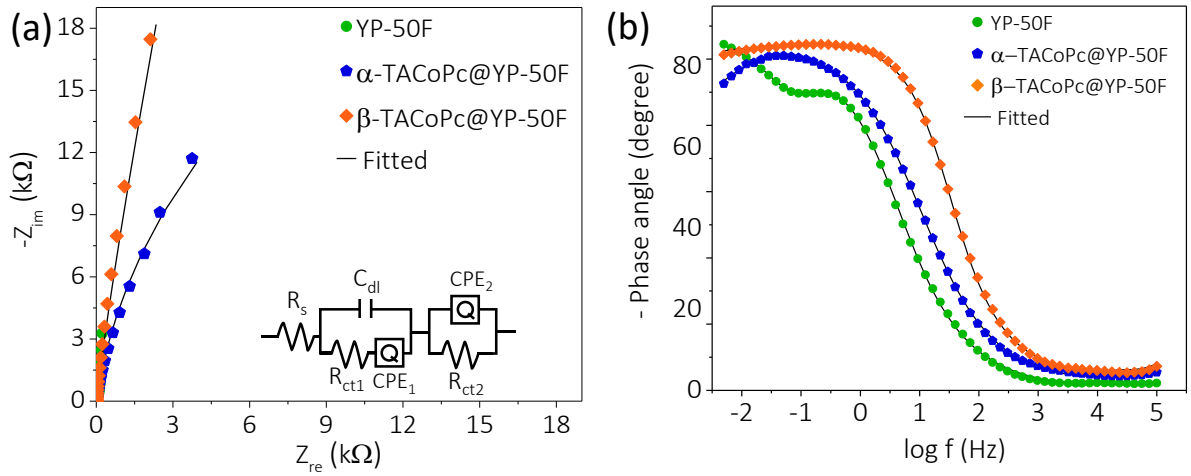

Figure S26 | Characteristic time constant analysis. (a) Nyquist plots and (b) Bode plots (log of frequency vs. phase angle) for YP-50, *α*-TACoPc@YP-50F and *β*-TACoPc@YP-50F electrodes at 0 V vs. OCV, acquired in the frequency range of 100 kHz to 5 mHz with a 10 mV (peak to peak) AC excitation signal. Inset of S26a shows the electrical equivalent circuit used in fitting the experimental EIS data.

As shown in the inset of Figure S26a, the impedimetric behavior of the best electrode (*β*-TACoPc@YP-50F) could be fitted with an electrically equivalent circuit, comprising a solution resistance (R_s = 2.61 Ω), a double-layer capacitance (C_{dl} = 78.12 nF), an electron-transfer resistance (R_{ct1} = 9.80 Ω and R_{ct2} = 88.08 Ω), and a constant-phase element (CPE_1 = 8.08 mF with n_1= 0.95 and CPE_2 = 61.81 mF with n_2 = 0.68).

Table S9 | Knee frequency and relaxation time of YP-50F and its composite electrodes with *α*-TACoPc and *β*-TACoPc determined using the electrochemical impedance spectroscopy (EIS) method. (Values are extracted from Figure 4f).

Electrodes	***"knee" or "onset" frequency (f_o) in (Hz)***	
	f_o	*$1/f_o$*
YP-50F	*3*	*333 ms*
α-TACoPc@YP-50F	*9*	*111 ms*
β-TACoPc@YP-50F	*32*	*31.2 ms*

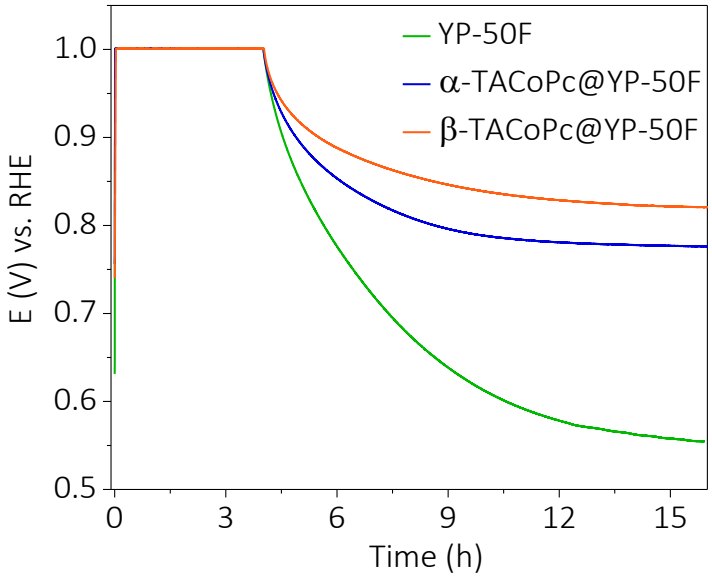

Figure S27│ Self-discharge profiles of *α*-TACoPc@YP-50F and *β*-TACoPc@YP-50F in a three-electrode configuration.

Table S10│ Performance metrics of the Supercapacitors.

Specific capacitances were measured by galvanostatic discharge method at a rate of 1 A/g, self-discharge currents and leak currents were determined for YP-50F and its composites with *α*-TACoPc and *β*-TACoPc electrodes as shown in Figure S27.

Electrode Materials	***YP-50F***	***α-TACoPc@YP-50F***	***β-TACoPc@YP-50F***
Open circuit voltage (OCV) vs. RHE	*0.63*	*0.75*	*0.74*
Specific capacitance ($F \cdot g^{-1}$)	*218*	*359*	*729*
Self-discharge current (μA)	30.10^{-3}	23.10^{-3}	19.10^{-3}
Leakage current ($mA \cdot F^{-1} \cdot V^{-1}$)	177.10^{-3}	124.10^{-3}	79.10^{-3}

16. Galvanostatic cycling in a 3-electrode cell

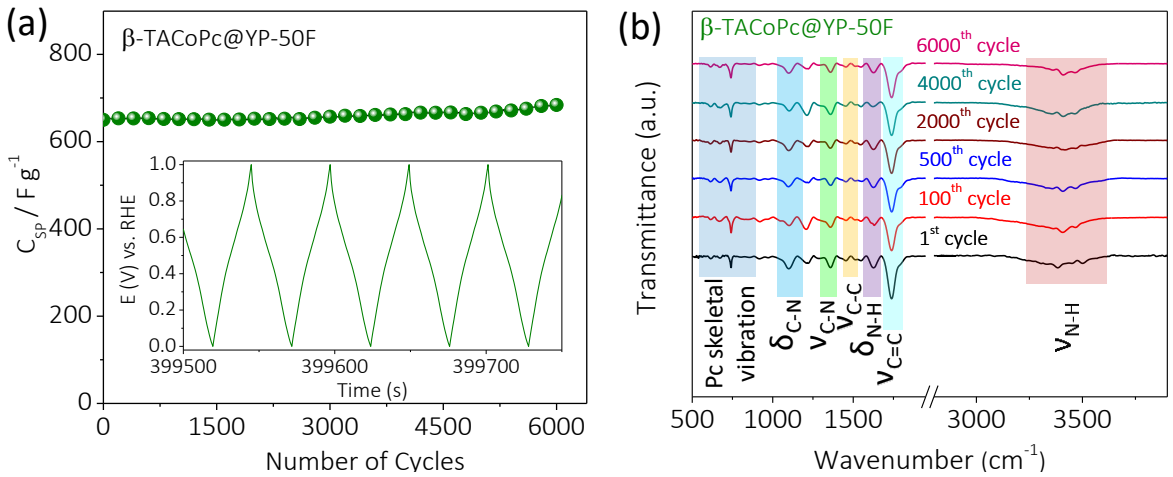

Figure S28 | Galvanostatic cycling. (a) Variation of specific capacitance with the number of cycles at 5.6 mA/cm^2 (10 A/g). Inset is a portion of the charge-discharge curves obtained during the 5th day of repetitive cycling. Supporting electrolyte is N_2 saturated 0.5 M H_2SO_4. (b) FTIR spectroscopy of *β*-TACoPc@YP-50F electrodes during extended cycling.

The stability of the *β*-TACoPc@YP-50F electrode was examined by continuous cycling at a current density of 5.6 mA cm^{-2} (10 A/g), as shown in Figure S28. Charge-discharge profiles remain almost unchanged, even after 6000 cycles (10,000 cycles are provided above for 2 electrodes in an asymmetric configuration), indicating that the electrode can be charged and discharged continuously without any significant loss in capacitance (Figure S28a). Moreover, the FTIR spectra of the *β*-TACoPc@YP-50F electrode demonstrate that the electrode is durable even after extended cycling for 6,000 cycles, as shown in Figure S28b.

17. Understanding the particular EDLC due to H-bonding effect

Table S11 | Capacitance of different types of electrode and $\Gamma_{(\alpha \text{ or } \beta)}(\gamma)$ value.

Types of electrodes	*Flat electrode*		*Porous electrode*	
	C (mF·cm^{-2})	*$\Gamma_{(\alpha \text{ or } \beta)}(\gamma)$*	*C (F·g^{-1})*	*$\Gamma_{(\alpha \text{ or } \beta)}(\gamma)$*
Bare	*0.068*	*1*	*180*	*1*
α-TACoPc	*0.553*	*8.13235294*	*323*	*1.79444444*
β- TACoPc	*1.410*	*20.5882353*	*675*	*3.75*

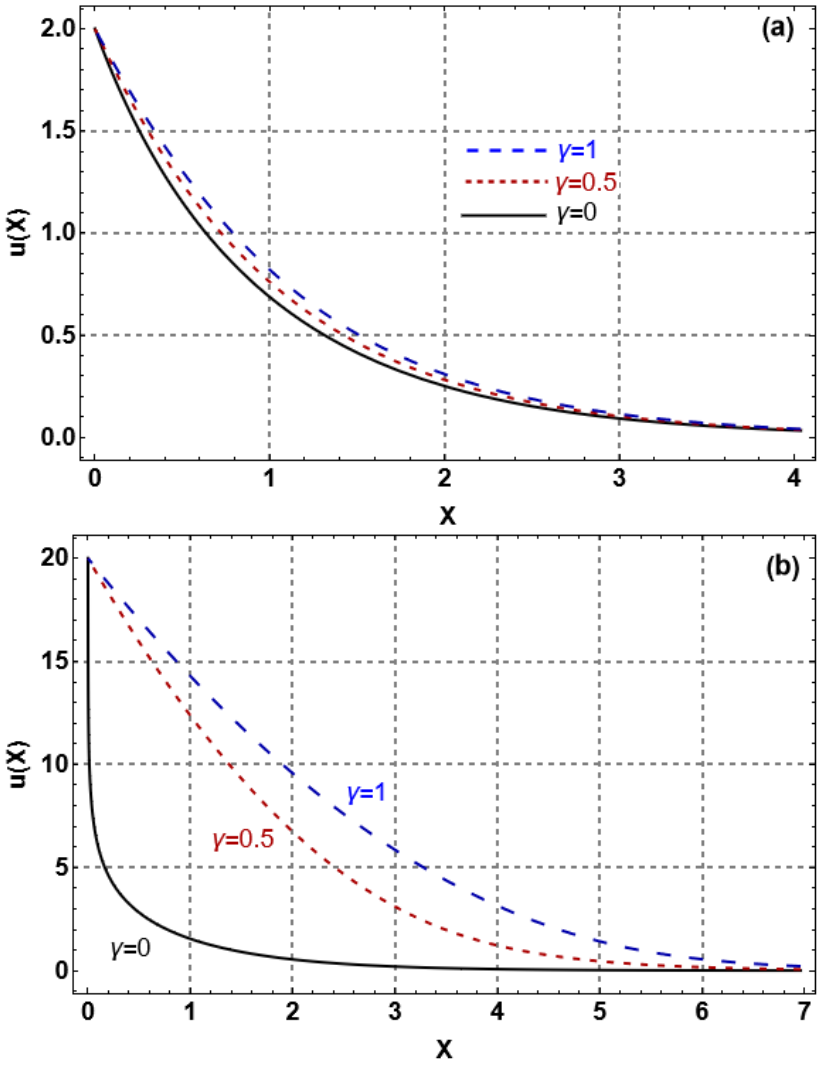

Figure 29 | The potential dependences on distance near the positive charged electrode with different values of γ parameter when u(X) at X=0 are (a) 2, and (b) 20.

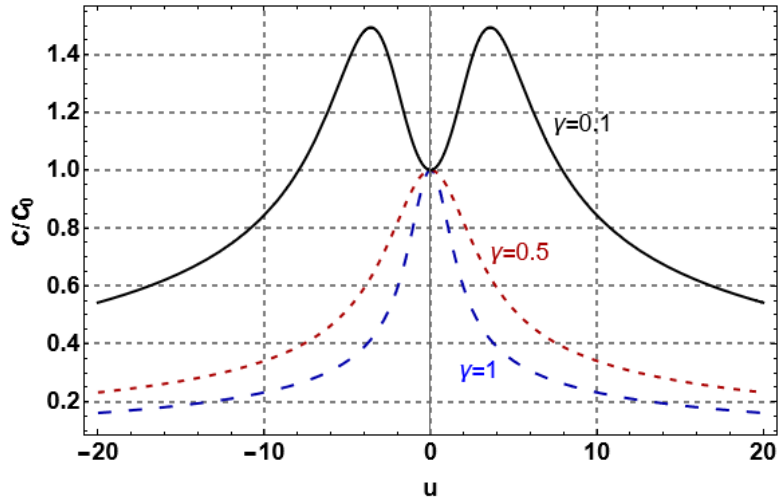

Figure S30 | The relative capacitance variation upon electrode potential with bell-shape and camel-shape at different values of γ.

Table S12 | The compactness parameter Γ(γ), compacity coefficient γ of different types of electrodes, and the potential shift u(X) at X=0.022, whereas X=0, $\Phi_0 = 2V$ or $u(X_0) = \frac{2e}{k_B T} = 79.212$.

Types of electrodes	*Flat electrode*				*Porous electrode*			
	$\Gamma(\gamma)$	$u(X)$	$\Phi(X)$	γ	$\Gamma(\gamma)$	$u(X)$	$\Phi(X)$	γ
Bare	*1*	*9.020*	*0.231 V*	*0*	*1*	*9.020*	*0.231 V*	*0*
α-TACoPc	*8.132*	13.282	*0.341 V*	5.230×10^{-6}	*1.794*	*20.897*	*0.536 V*	8.774×10^{-6}
β-TACoPc	*20.588*	13.279	*0342 V*	5.244×10^{-6}	*3.75*	*15.329*	*0.394 V*	5.639×10^{-6}

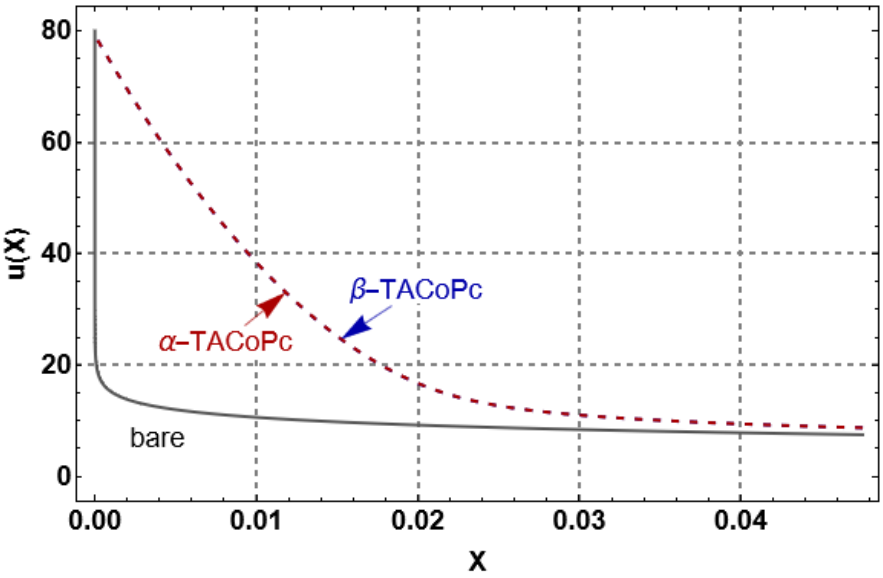

Figure S31 | The potential dependences on distance near the bare, and alpha (or beta) modified positive charged on flat electrode.

References:

1. J. Alzeer, P. J. C. Roth, N. W. Luedtke, *Chem. Commun.* **2009**, 1970.
2. K. Al-lami, N. N. Majeed, A. H. Al-mowali, **2013**, *3*, 59–68.
3. A. Cidlina, V. Novakova, M. Miletin, P. Zimcik, *Dalton Trans.* **2015**, *44*, 6961–6971.
4. M. N. Yarasir, M. Kandaz, O. Güney, B. Salih, *Spectrochim. Acta - Part A Mol. Biomol. Spectrosc.* **2012**, *93*, 379–383.
5. Obirai, J. & Nyokong, T. *Electrochim. Acta* **2005**, *50*, 3296–3304.
6. J. Obirai, T. Nyokong, *Electrochim. Acta* **2005**, *50*, 5427–5434.
7. A. Ogunsipe, T. Nyokong, *J. Mol. Struct.* **2004,** *689*, 89–97.
8. M. H. Moinuddin Khan, K. R. Venugopala Reddy, J. Keshavayya, Fasiulla, S. Raghavendra, *Green Chem. Lett. Rev.* **2009**, *2*, 77–85.
9. T. Mugadza, T. Nyokong, *Electrochim. Acta* **2010**, *55*, 6049–6057.
10. T. Mugadza, T. Nyokong, *Electrochim. Acta* **2009**, *54*, 6347–6353.
11. N. Kobayashi, H. Miwa, V. N. Nemykin, *J. Am. Chem. Soc.* **2002**, *124*, 8007–8020.
12. K. P. Madhuri, N. S. John, *ChemistrySelect* **2019**, *4*, 7292–7299.
13. R. Georgescu, C. Boscornea, I. Calinescu, R. State, **2016**.
14. F. Cong, et al., *Dye. Pigment.* **2005**, *66*, 149–154.
15. X.F. Zhang, X. Li, L. Niu, L. Sun, L. Liu, *J. Fluoresc.* **2009**, *19*, 947–954.
16. T. Yanai, D. P. Tew, N. C. Handy, *Chem. Phys. Lett.* **2004**, *393*, 51–57.

17. M.J. Frisch, G.W. Trucks, H.B. Schlegel, G.E. Scuseria., M.A. Robb, J.R. Cheeseman, G. Scalmani, V. Barone, B. Mennucci, G.A. Petersson, H. Nakatsuji, M. Caricato, X. Li, H.P. Hratchian, A.F. Izmaylov, J. Bloino, G. Zheng, J.L. Sonnenberg, M. Hada, M. Ehara, K. Toyota, R. Fukuda, J. Hasegawa, M. Ishida, T. Nakajima, Y. Honda, O. Kitao, H. Nakai, T. Vreven, J.A. Montgomery, J.J.E. Peralta, F. Ogliaro, M. Bearpark, J.J. Heyd, E. Brothers, K.N. Kudin, V.N. Staroverov, T. Keith, R. Kobayashi, J. Normand, K. Raghavachari, A. Rendell, J.C. Burant, S.S. Iyengar, J. Tomasi, M. Cossi, N. Rega, J.M. Millam, M. Klene, J.E. Knox, J.B. Cross, V. Bakken, C. Adamo, J. Jaramillo, R. Gomperts, R.E. Stratmann, O. Yazyev, A.J. Austin, R. Cammi, C. Pomelli, J.W. Ochterski, R.L. Martin, K. Morokuma, V.G. Zakrzewski, G.A. Voth, P. Salvador, J.J. Dannenberg, S. Dapprich, A.D. Daniels, O. Farkas, J.B. Foresman, J. V Ortiz, Cioslowski, D.J. and Fox, I. Gaussian Wallingford CT., *Gaussian 09, Revis. C.01*. **2010**.
18. S. Grimme, J. Antony, S. Ehrlich, H. Krieg, *J. Chem. Phys.* **2010**, *132*, 154104 (1-19).
19. G. Stefan, E. Stephan, G. Lars, *J. Comput. Chem.* **2011,** *32*, 1456–1465.
20. F. Glendening, E. D, Reed, A. E, Carpenter, J, E, Weinhold, *NBO Version 3.0*, **2003.**
21. K. Momma, F. Izumi, *J. Appl. Crystallogr.* **2011**, *44*, 1272–1276.
22. G. A. Jeffrey, *An Introduction to Hydrogen Bonding*, eds (*Oxford University Press*), **1997**.
23. S. Thomas, *Angew. Chemie Int. Ed.* **2002**, *41*, 48–76.
24. P. Froimowicz, K. Zhang, H. Ishida, *Chem. - A Eur. J.* **2016**, *22*, 2691–2707.
25. P. Che, et al. *Chem. Commun.* **2015**, *51*, 1077–1080.
26. B. D. Fleming, S. Praporski, A. M. Bond, L. L. Martin, *Langmuir* **2008**, *24*, 323–327.
27. A. S. Viana, M. Kalaji, L. M. Abrantes, *Langmuir* **2003**, *19*, 9542–9544.
28. K. Nakano, T. Yoshitake, Y. Yamashita, E. F. Bowden, *Langmuir* **2007**, *23*, 6270–6275.
29. Z. O. Makinde, M. Louzada, P. Mashazi, T. Nyokong, S. Khene, *Appl. Surf. Sci.* **2007**, *425*, 702–712 (2017).
30. J. Bae, M. K. Song, Y. J. Park, J. M. Kim, M. Liu, Z. L. Wang, *Angew. Chemie* **2011**, *123*, 1721–1725.
31. Q. Wang, X. Wang, J. Xu, X. Ouyang, X. Hou, D. Chen, R. Wang, G. Shen, *Nano Energy* **2014**, *8*, 44–51.
32. H. Wu, Z. Lou, H. Yang, G. Shen, **2015**, *1*, 1921–1926.
33. D. Bruce et al., *J. Phys. Chem. C* **2007**, *111*, 14925-14931.

34. J. Zhu, J. et al. *Carbon N. Y.* **2011**, *49*, 1900–1905.
35. X. Zhang, et al. *Nat. Commun.* **2017**, *8*, 14675.
36. M. Shrestha, et al. *J. Energy Storage* **2017**, *13*, 206–210.
37. T. I. Singh, G. Rajeshkhanna, T. Kshetri, N. H. Kim, J. H. Lee, *J. Mater. Chem. A* **2020**, *8*, 26158–26174.
38. H. Li, J. Lang, S. Lei, J. Chen, K. Wang, L. Liu, T. Zhang, W. Liu, X. Yan, *Adv. Funct. Mater.* **2018**, *28*, 1–12.
39. D. S. Kong, J. M. Wang, H. B. Shao, J. Q. Zhang, C. N. Cao, *J. Alloys Compd.* **2011**, *509*, 5611–5616.
40. K. Yang, K. Cho, S. Kim, *Sci. Rep.* **2018**, *8*, 1–7.
41. P. L. Taberna, P. Simon, J. F. Fauvarque, *J. Electrochem. Soc.* **2003**, *150*, A292.
42. Y. Yoo, M. S. Kim, J. K. Kim, Y. S. Kim, W. Kim, *J. Mater. Chem. A* **2016**, *4*, 5062–5068.
43. A. C. Rodrigues, E. L. Da Silva, S. F. Quirino, A. Cuña, J. S. Marcuzzo, J. T. Matsushima, E. S. Gonçalves, M. R. Baldan, *Mater. Res.* **2018**, *22*, 1–9.
44. X. Wang, T. Song, *New J. Chem.*, **2016**, *40*, 8006-8011.
45. E. Mourad, L. Coustan, P. Lannelongue, D. Zigah, A. Mehdi, A. Vioux, S. A. Freunberger, F. Favier, O. Fontaine, *Nat. Mater.* **2017**, *16*, 446–454.
46. M. F. El-kady, R. B. Kaner, *Nat. Commun.* **2013**, *4*, 1475–1479.